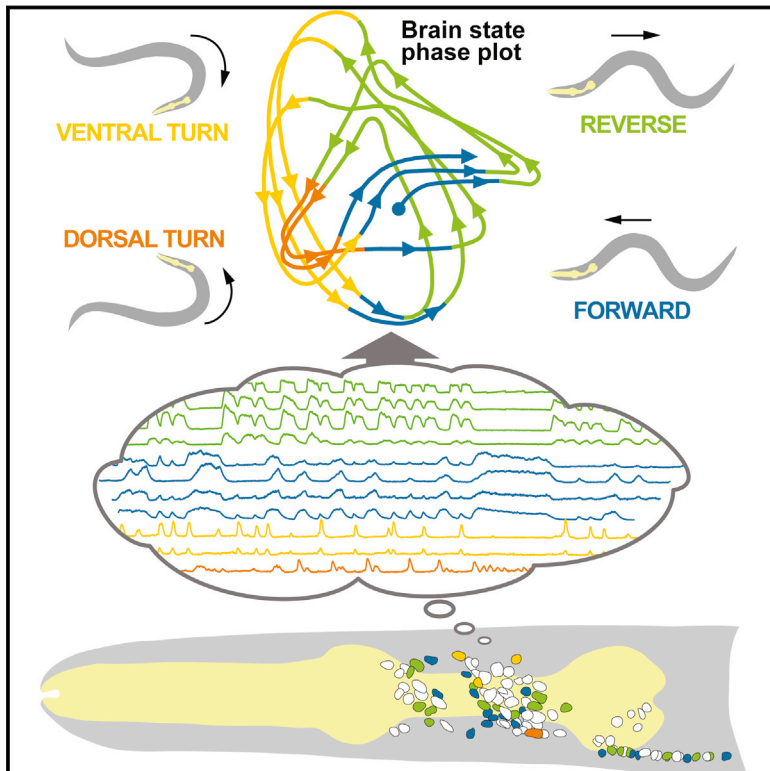


# Global Brain Dynamics Embed the Motor Command Sequence of *Caenorhabditis elegans*

## Graphical Abstract



## Authors

Saul Kato, Harris S. Kaplan, Tina Schrödel, ..., Eviatar Yemini, Shawn Lockery, Manuel Zimmer

## Correspondence

zimmer@imp.ac.at

## In Brief

Simultaneously recording the activity of nearly all neurons in the *C. elegans* brain reveals that most active neurons share information by engaging in coordinated, dynamical network activity that corresponds to the sequential assembly of motor commands.

## Highlights

- Most active neurons in the brain participate in coordinated dynamical activity
- Smooth, cyclical dynamics continuously represent action sequences and decisions
- Internal representation of behavior persists when decoupled from its execution
- Brain dynamics provide a robust scaffold for sensory-driven action selection



# Global Brain Dynamics Embed the Motor Command Sequence of *Caenorhabditis elegans*

Saul Kato,<sup>1,4</sup> Harris S. Kaplan,<sup>1,4</sup> Tina Schrödel,<sup>1,4</sup> Susanne Skora,<sup>1</sup> Theodore H. Lindsay,<sup>2,5</sup> Eviatar Yemini,<sup>3</sup> Shawn Lockery,<sup>2</sup> and Manuel Zimmer<sup>1,\*</sup>

<sup>1</sup>Research Institute of Molecular Pathology IMP, Vienna Biocenter VBC, Dr. Bohr-Gasse 7, 1030 Vienna, Austria

<sup>2</sup>Institute of Neuroscience, University of Oregon, Eugene, OR 97403, USA

<sup>3</sup>Department of Biochemistry and Molecular Biophysics, Howard Hughes Medical Institute, Columbia University Medical Center, New York, NY 10032, USA

<sup>4</sup>Co-first author

<sup>5</sup>Present address: Division of Biology and Biological Engineering, California Institute of Technology, Pasadena, CA 91125, USA

\*Correspondence: [zimmer@imp.ac.at](mailto:zimmer@imp.ac.at)

<http://dx.doi.org/10.1016/j.cell.2015.09.034>

## SUMMARY

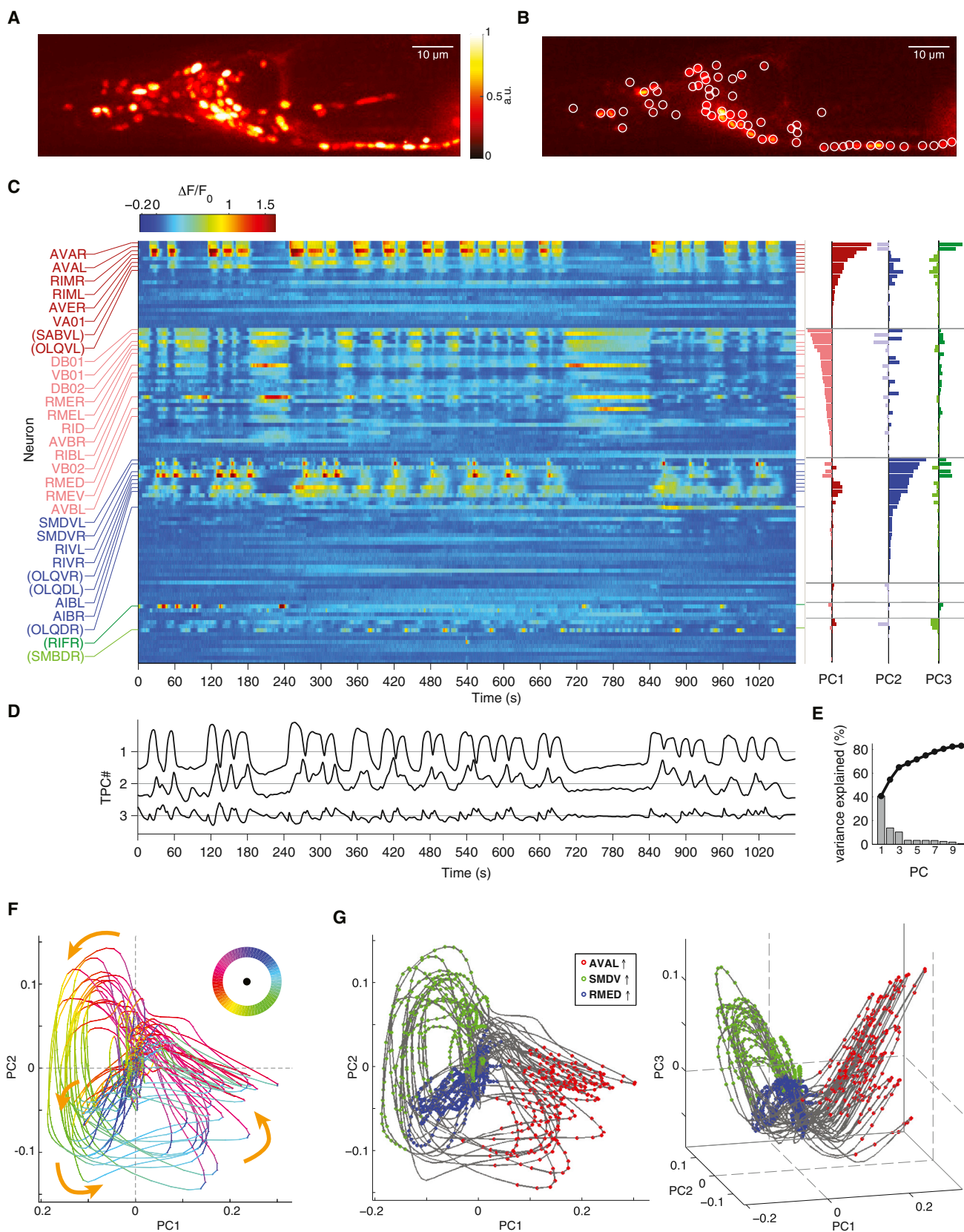
While isolated motor actions can be correlated with activities of neuronal networks, an unresolved problem is how the brain assembles these activities into organized behaviors like action sequences. Using brain-wide calcium imaging in *Caenorhabditis elegans*, we show that a large proportion of neurons across the brain share information by engaging in coordinated, dynamical network activity. This brain state evolves on a cycle, each segment of which recruits the activities of different neuronal sub-populations and can be explicitly mapped, on a single trial basis, to the animals' major motor commands. This organization defines the assembly of motor commands into a string of run-and-turn action sequence cycles, including decisions between alternative behaviors. These dynamics serve as a robust scaffold for action selection in response to sensory input. This study shows that the coordination of neuronal activity patterns into global brain dynamics underlies the high-level organization of behavior.

## INTRODUCTION

Behavior is composed of individual motor actions and motifs, such as limb movements or gaits, which do not achieve organismal goals unless they are orchestrated into longer-lasting action sequences and behavioral strategies, like navigation, grooming, or courtship (Anderson and Perona, 2014; Gray et al., 2005; Seeds et al., 2014). Ethologists often make quantitative descriptions of this higher-level organization using state transition diagrams, consisting of distinct, repeatable high-level motor states and switches between them (Anderson and Perona, 2014). The brain's representation of behavior must account for both detailed metrics of individual actions (e.g., strength and extent of movement or speed of gait), as well as for their higher level orchestration. Identifying how these aspects of behavior correspond to measurable neural activity is a necessary step toward understanding how the brain encodes and produces

behavior. Recent studies in invertebrate motor ganglia and mammalian cortex show that selection, execution, and shaping of motor programs correspond to neural activity patterns across large neuronal populations. These studies show that, despite the participation of hundreds of sampled neurons, their activity is coordinated, and meaningful signals can thus be reduced to far fewer dimensions. Moreover, neuronal populations encode information dynamically (Briggman et al., 2005; Bruno et al., 2015; Churchland et al., 2012; Cunningham and Yu, 2014; Harvey et al., 2012; Jin et al., 2014; Mante et al., 2013). For practical reasons, recordings in these studies have been performed over short intervals that encompass individual motions or brief behavioral tasks. Hence, the neuronal mechanisms that govern the continuous control of behavior and its time course, encompassing long-lasting and repeated action sequences, remain enigmatic. Furthermore, approaches have been typically limited by the need to average across trials or to sub-sample from local brain regions or motor ganglia. Recently, the first brain-wide single-cell-resolution functional imaging studies, in zebrafish and fly larvae and adult *C. elegans*, revealed motor-related population dynamics correlated across distant brain regions. These data suggest that behaviorally relevant neural representations might occur at the level of global population dynamics and highlight the benefit of brain-wide sampling (Ahrens et al., 2012, 2013; Lemon et al., 2015; Panier et al., 2013; Prevedel et al., 2014; Schrödel et al., 2013).

The nematode *C. elegans* is an attractive model system to address these problems, due to its stereotypic nervous system of just 302 identifiable neurons grouped into 118 anatomical symmetry classes (White et al., 1986). However, prior to the availability of whole-brain imaging, past studies had not explored distributed or population dynamics in *C. elegans*. Instead, identified interneurons and pre-motor neurons have been described as dedicated encoders of specific sensory inputs or motor outputs and are commonly placed in a context of isolated sensory-to-motor pathways (see the following references for examples: Chalasani et al., 2007; Donnelly et al., 2013; Gray et al., 2005; Ha et al., 2010; Iino and Yoshida, 2009; Kimata et al., 2012). However, these pathways largely overlap and are embedded in a horizontally organized and recurrently connected neuronal wiring diagram (Varshney et al., 2011; White et al., 1986). Moreover, recent functional imaging



(legend on next page)

studies revealed that many of these circuit elements encode motor rather than sensory related signals (Gordus et al., 2015; Hendricks et al., 2012; Laurent et al., 2015; Li et al., 2014; Luo et al., 2014). Taken together, these considerations argue against separable feed-forward sensory pathways and instead support the hypothesis that sensorimotor processing is performed by distributed, shared networks operating on widespread motor representations.

In the present study, we provide evidence for this hypothesis by showing that many neurons in the *C. elegans* brain participate in a pervasive dynamic population state, collectively representing the major motor commands of the animal. The time evolution of the neural state is directional and cyclical, corresponding to the sequential order of the animals' repeated actions. These network dynamics interface with sensory representations as early as at the first synapse downstream of sensory neurons and provide a robust scaffold for sensory inputs to modulate behavior. Our work suggests that high-level organization of behavior is encoded in the brain by globally distributed, continuous, and low-dimensional dynamics.

## RESULTS

### Brain-wide Activity Evolves on a Low-Dimensional Attractor-like Manifold

We performed whole-brain single-cell-resolution  $\text{Ca}^{2+}$  imaging with a pan-neuronally expressed nuclear  $\text{Ca}^{2+}$  sensor in animals immobilized in a microfluidic device (Schrödel et al., 2013). In each animal ( $n = 5$ ), we recorded the brain activity under environmentally constant conditions for 18 min at a rate of  $\sim 2.85$  volumes per second. The imaging volume spanned all head ganglia, including most of the worm's sensory neurons and interneurons, as well as all head motor neurons and the most anterior ventral cord motor neurons (White et al., 1986) (Figures 1A and 1B). In each recording, we detected 107–131 neurons and were able to determine the cell class identity of most of the active neurons. Figures 1C and S1A show a typical multi-neuron time series during which a large proportion of imaged neurons exhibited discernable  $\text{Ca}^{2+}$ -activity patterns. We performed principal components analysis (PCA) on the time derivatives of the normalized  $\text{Ca}^{2+}$  traces (Figures 1C–1E). This method produces neuron weight vectors, termed principal components (PCs); here, PCs are calculated based on the covariance structure found in the normalized data (Jolliffe, 2002). For each PC, a corresponding time series (temporal PC) was calculated by taking the weighted average of the full multi-neural time series. Temporal PCs repre-

sent signals shared by neurons that cluster based on their correlations. We found a low-dimensional, widely shared, dominant signal: the first three PCs accounted for 65% of the full dataset variance (Figure 1E). We performed PCA on the time derivatives of  $\text{Ca}^{2+}$  traces because the resulting PCs produced more spatially organized state space trajectories, described below.

The time integral of temporal PC1 displayed a strong oscillatory time course with variable period, sharp transitions, and prolonged plateaus and troughs. This pattern derived from the antagonistic activity of two groups of interneurons and motor neurons (Figure 1C, right) previously implicated in controlling the switch between forward- and backward-directed crawling (Table S1 summarizes published results). Neurons previously reported to have opposing roles were observed to have opposing signs of their PC1 weights—e.g., AVA promoting backward crawling and AVB promoting forward crawling. PC2 and PC3 received high contributions from head motor neurons. Two of these neurons (SMDV and RIV) have been implicated in postural changes required for navigational re-orientation maneuvers (termed omega turns) (Gray et al., 2005). However, the neuronal weights of all three PCs indicated contributions from many neurons (Figure 1C). PC1–3 weights and their variance contributions were consistent across the five datasets (Figures S2A–S2D).

The phase plot of temporal PC1–3 showed that the neural state's time evolution was cyclical—i.e., the same states were repeatedly revisited within a trial, such that successive trajectory cycles formed spatially coherent bundles (Figure 1F and Movie S1). Consequently, the entire neural state trajectory traced out a manifold, which is defined here as the sub-volume in PCA space occupied by the neural state trajectory. When mapped onto the neural trajectory, individual neurons' activity rise and fall phases occupied class-specific sub-regions on the manifold (Figures 1G and S1B). All five recordings displayed a similarly structured manifold (Figure S2E). Thus, a large group of interneurons and motor neurons produces a cyclical, low-dimensional population state time-varying signal.

### Interneurons and Head Motor Neurons Reliably Encode Motor State and Graded Motion Parameters

Next, we aimed for a functional interpretation of the neural state manifold and its properties. Each manifold sub-region was labeled specifically and consistently by different subsets of neurons, some of which have been previously implicated in the action sequence termed a pirouette (Table S1), which is central to navigation (Gray et al., 2005; Pierce-Shimomura et al., 1999). During pirouettes, worms switch transiently from

#### Figure 1. Brain-wide Activity Is Organized in a Low-Dimensional, Cyclical Neural State Space Trajectory

- (A) Maximum intensity projection of a representative sample recorded under constant conditions.  
 (B) Single z plane overlaid with segmented neuronal regions.  
 (C) Heat plot of fluorescence ( $\Delta F/F$ ) time series of 109 segmented head neurons, one neuron per row. Labeled neurons indicate putative cell IDs. Ambiguous neuron IDs are in parentheses (see Figure S1 for additional candidates). Neurons are colored and grouped by their principal component (PC1–3) weights and signs, which are shown by the bar plots on the right.  
 (D) Integrals of the first three temporal PCs.  
 (E) Variance explained by first ten PCs, black line indicates cumulative variance explained.  
 (F) Phase plot of first two temporal PCs colored by direction of time evolution indicated by color key.  
 (G) Phase plots of first two (left) and first three (right) temporal PCs. Colored balls indicate  $\text{Ca}^{2+}$  rises of three example neurons indicated by legend.  
 See also Movie S1 and Figures S1 and S2.

forward- to backward-directed crawling, termed a reversal (Figures 2A and 2B). They then resume forward crawling with a concomitant turn along the dorsal or ventral body axis; worms crawl lying on their left or right side (Figures 2C and 2D). We performed  $\text{Ca}^{2+}$  imaging experiments of representative neurons in freely moving worms while simultaneously recording their behavior with an infrared (IR) camera (Faumont et al., 2011). We selected neurons based on their PC weights and availability of specific promoters to drive GCaMP expression. As with brain-wide imaging experiments, animals were recorded 5–10 min after removal from food, a paradigm in which pirouettes contribute to a local search strategy (Gray et al., 2005). Behavioral analysis of the IR movies showed that reversal initiations were each preceded by a reduction in crawling speed (slowing bout), though 20% of slowing bouts did not lead to a reversal (Figures S3A and S3B). We thus defined slowing as an additional behavioral state and represent pirouettes together with forward crawling as action sequences composed of forward run, slowing, reversal, resume forward via dorsal turn, and resume forward via ventral turn actions, which is depicted in a state transition diagram (Figure 2E).

We first examined  $\text{Ca}^{2+}$  dynamics in neurons with high positive or negative PC1 weight. An example trace of RIM neurons is shown in Figure 2F. We found that the  $\text{Ca}^{2+}$  signals of RIM resided in stable low states during forward-directed crawling and that  $\text{Ca}^{2+}$  rises occurred exclusively during reversals (Figure 2F). The slope of these signals correlated with the speed of reverse crawling (Figure 2G). Although reversals are of variable duration (Gray et al., 2005; Pokala et al., 2014) (Figure S3B), RIM  $\text{Ca}^{2+}$  rise onsets precisely aligned with reversal start, and RIM  $\text{Ca}^{2+}$  fall onsets aligned with reversal end. This relationship was highly reliable—approximately 90% of reversals were associated with a detectable RIM  $\text{Ca}^{2+}$  rise phase (Figure 2H, top), and the remainders were very short reversals where small  $\text{Ca}^{2+}$  signals might have been occluded by noise (Figure 2F). All clearly discernible RIM  $\text{Ca}^{2+}$  rises above our signal-to-noise threshold occurred during reversals. We found such a relationship of  $\text{Ca}^{2+}$  rise and fall phases with respect to reversal events for all tested neurons with positive PC1 weight (RIM, AVA, AVE, AIB), while neurons with negative PC1 weight (RIB, AVB, RMEV) showed the inverse relationship (Figures 2H and S3C–S3H). All these neurons' activities changed as reliably as RIM at both forward-reverse and reverse-forward transitions.

Besides this common property of PC1 neurons, class-specific relationships between neuronal activity and locomotion were revealed by freely moving  $\text{Ca}^{2+}$  imaging. RIM and AVA  $\text{Ca}^{2+}$  rise slopes, and AVE  $\text{Ca}^{2+}$  signal magnitude, were graded and correlated with reverse crawling speed (Figures 2G, S3I, and S3J). Unlike RIM, AVA, and AVE, the activity of AIB did not show strong correlations with reverse crawling speed (Figures S3E and S3K); however, small AIB  $\text{Ca}^{2+}$  transients co-occurred with forward slowing bouts, even when no reversal followed (Figures S3E and S3Q). Consistent with this, AIB  $\text{Ca}^{2+}$  rise phases preceded the forward-to-reversal transition by  $\sim 1$  s on average (Figure 2H). The continuous activity of AVB and RIB, unlike RMEV, showed strong correlations with forward crawling speed (Figures S3L–S3P; see also Li et al., 2014). Consistent with this, AVB and

RIB  $\text{Ca}^{2+}$  fall phases preceded the forward to reverse transition by  $\sim 1$  s on average (Figure 2H).

Next, we examined the activity of SMDV head motor neurons as representative neurons with strong PC2/3 weight. Resumption of forward crawling begins with a dorsal or ventral bend, which was biased (71%/29%) in the ventral direction. The head flexure during post-reversal turns is graded and increased compared to normal forward crawling, especially for ventral bends (Figure 3A). SMDV exhibited  $\text{Ca}^{2+}$  rises at the transition from reverse to forward crawling; importantly, these rises occurred exclusively during ventrally and not dorsally directed events (Figures 3B–3D). The magnitude of these signals correlated with ventral head-bending flexure (Figure 3E).

The major qualitative divergence in neural activity patterns between the freely moving single neuron and restrained whole-brain setups that we observed was the absence, in freely moving worms, of prolonged high phases in neurons with positive PC1 weight. Using RIM as an exemplar, we first ruled out that this difference was a consequence of nuclear localization of the  $\text{Ca}^{2+}$  reporter used in whole-brain imaging (Figures S3R–S3T). We then dissociated the two major differences in these experimental conditions by performing experiments in either pharmacologically or physically immobilized worms. While low doses of the paralyzing agent tetramisole caused RIM high phases in conjunction with prolonged slowly executed reversals, physical immobilization alone also caused RIM high phases (Figures S3U–S3X). These data suggest that impeded motor execution leads to a prolongation of the reversal, which is correlated with sustained  $\text{Ca}^{2+}$  levels in reversal-promoting neurons.

In summary, the investigated neuronal activities showed both (1) sharp transitions depending on discrete motor state (i.e., forward versus backward crawling, ventral versus dorsal turning direction) and (2) graded information about motion parameters (i.e., forward and reverse crawling speed and head bending flexure). Acute motor state reliably matched the activities of the associated neurons on a single event basis. Importantly, when examining neuron activity periods mapped onto the neural state manifold, we observed that neurons encoding the same behavioral state in freely moving animals shared the same manifold sub-regions with rare exception (Figure S1B).

### Manifold Branches and Bundles Exhibit Distinct Neuronal Recruitment Patterns

Having determined that the neural state manifold is a composite of motor related signals, we next aimed for a quantitative description thereof. We first segmented the global brain cycle into four behaviorally relevant phases using the left AVA neuron (AVAL) as a reference: a trough in AVAL  $\text{Ca}^{2+}$  defined the LOW state, a  $\text{Ca}^{2+}$  increase the RISE state, a  $\text{Ca}^{2+}$  plateau the HIGH state, and a  $\text{Ca}^{2+}$  decrease the FALL state (Figure 4A). We chose this single neuron class because it is among the highest PC1 contributors, participated in every brain cycle, and, unlike temporal PCs, exhibited sharply discernible transitions; however, other strongly PC1-contributing neurons such as RIM could also be used for this purpose. We validated that the appearance of lasting plateau and smooth transition states was not due to temporal filtering effects of  $\text{Ca}^{2+}$  imaging: all four states were readily discernible in AVA membrane voltage recordings, and

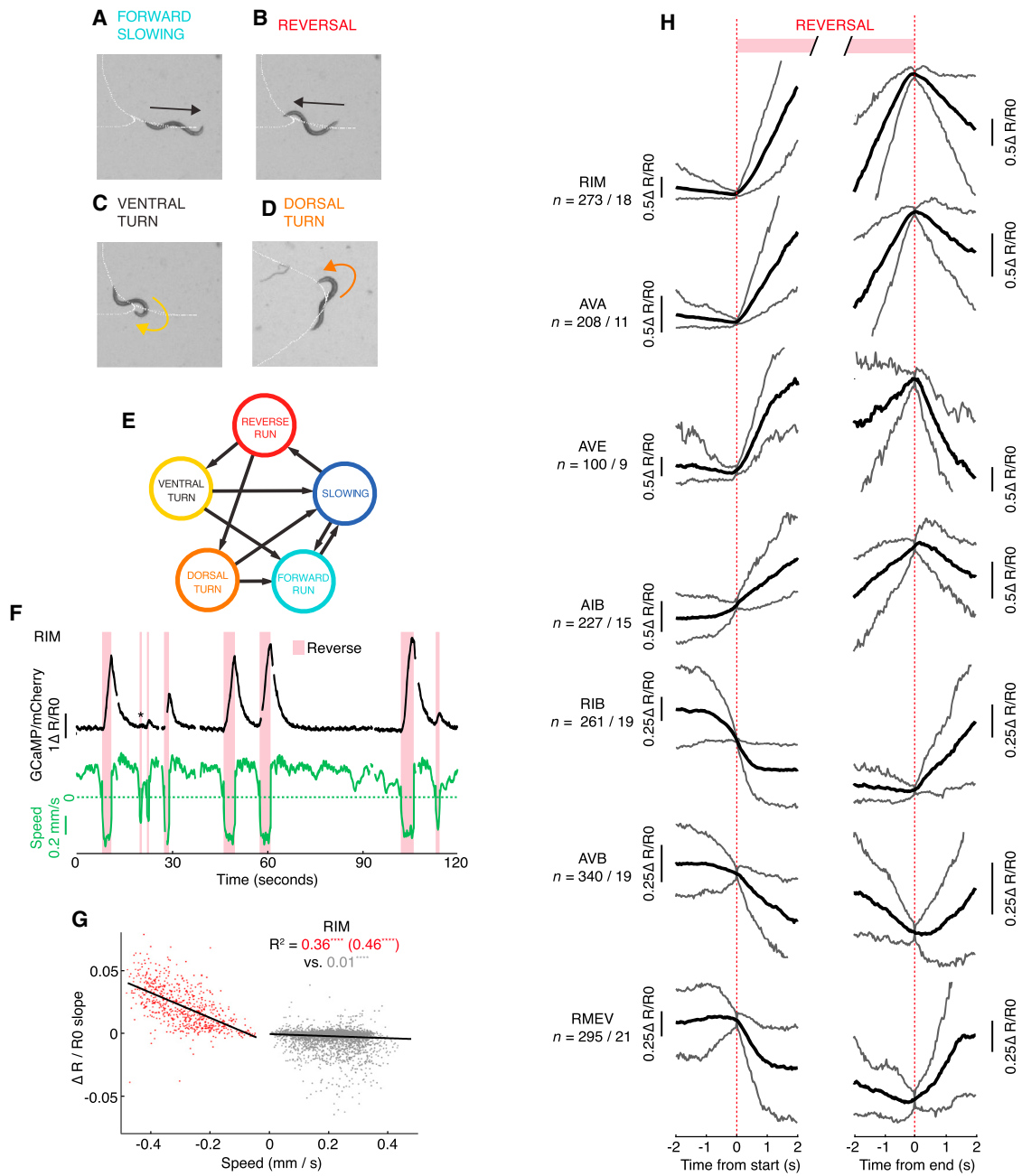


**Figure 2. Distributed Encoding of Motor State and Crawling Speed by Interneurons in Freely Moving Worms**

(A–D) Motor states of pirouette action sequence. White dotted lines show crawling trajectory. Arrows indicate crawling direction.

(E) Behavioral state transition diagram indicating motor states as circles and possible transitions as arrows.

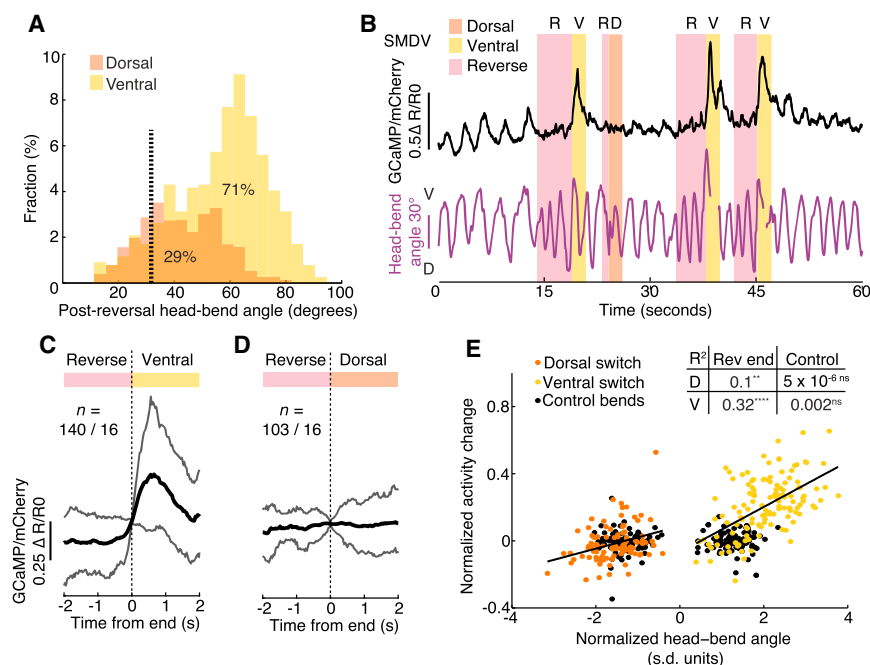
(F–H)  $Ca^{2+}$  imaging in freely moving animals.

(F) Example trace showing RIM activity as normalized GCaMP/mCherry fluorescence ratio (black) and corresponding crawling speed (green). Pink bars overlay reverse crawling periods. Asterisk indicates reversal with no detectable RIM activity peak.

(G) Regression analysis of crawling speed versus RIM  $Ca^{2+}$  signal slope.  $R^2$  indicates goodness of linear fit for instantaneous and maximum (in parentheses) reverse speed (red) and instantaneous forward speed (gray). Permutation test  $p$  value \*\*\*\* $p < 0.0001$  indicates probability that correlation was obtained by chance.

(H) Average  $Ca^{2+}$  signals of the indicated neurons triggered to reversal start (left) or end (right). Upper and lower traces represent 90<sup>th</sup> and 10<sup>th</sup> percentile of all data, respectively. Number of recorded worms and reversal events are indicated.

See also Figure S3.



selected head-bend peaks during regular forward movement.  $R^2$  indicates goodness of linear fits to ventral (V), dorsal (D), and respective control groups. Permutation test p values (\*\*\*\* $p < 0.0001$ , \*\* $p < 0.01$ , <sup>ns</sup> not significant) indicate probability that  $R^2$  value was obtained by chance.

we calculated an estimate of low-pass filtering caused by nuclear  $Ca^{2+}$ -imaging, producing a maximum delay in signal peaks of less than 1.1 s (Figure S4). Although neurons with a common relationship to behavior were recruited to the same sub-regions of the manifold, their precise phase onsets and offsets varied. In order to quantify this observation, for each onset of RISE and FALL, we created a vector containing the phase delays of all recruited neurons (Figure S5) (see Supplemental Experimental Procedures for details). Across the five datasets, we detected 121 RISE and 123 FALL transitions and observed characteristic phase delay distributions for each neuronal class (Figure S5). Next, we searched for structure across neuronal classes by performing k-means clustering separately for the RISE and FALL phase timing vectors; we found that both could be significantly clustered into two groups each, which we termed RISE1/2 and FALL1/2, respectively. RISE1 differed from RISE2 mostly based on different timing of neurons; e.g., AIB and RIB activity exhibited phase advances during RISE1 (Figure S5). FALL1 and FALL2 mostly differed by mutually exclusive head motor neuron recruitments, SMDV/RIV versus RMD/ventral ganglion head motor neuron (likely SMB, SMDD, or RMF) (Figure S5). The precise ordering detected by this method may be affected by differential  $Ca^{2+}$  dynamics in different cells; however, the reproducible clustering would be preserved. Using this six-state classification (LOW, RISE1/2, HIGH, and FALL1/2), we labeled the neural state trajectory and found that each state classifies a distinct bundle of trajectory segments (Figures 4A and 4B and Movie S2). Thus, the two methods (PCA and phase timing analysis) revealed the same dynamical structure in the neural data. Bundle classification enabled us to calculate average neural state trajectories illus-

trating the canonical brain cycle (Figure 4C). Note that, without this single-trial clustering analysis, the cycle-averaged trajectory would be reduced to a single loop in neural state space. Furthermore, bundle classification enabled us to estimate a contour surface of the manifold (Figure 4D and Movie S3), where the extents correspond to the standard deviations (SDs) by which the trajectory path diverges from the canonical (average) path. The trajectory segments across all cycles are strongly bundled; the mean pairwise distance of points across any two phase-registered trajectory time points within a bundle is  $\sim 10\%$  of the diameter of the full trajectory, and their mean angular divergence is  $22^\circ$  versus  $90^\circ$  expected from uncorrelated orientations. In summary, we find that many active neurons across the brain are tightly bound to reproducible and smooth population dynamics.

### The Motor Command Sequence Is Embedded in Neural State Space

Remarkably, the relationships neurons exhibited with behavioral transitions (Figures 2H, 3C, and 3D) matched their phase relationships with the six state global brain cycle without exception. Assembling all of the neuronal-behavioral correlate information gathered via  $Ca^{2+}$  imaging in freely moving worms enabled us to unambiguously map the worm's major motor command states onto separate bundles of the neural state manifold (Figures 4B–4E)—RISE1 or RISE2, in conjunction with HIGH, correspond to reversals, with HIGH corresponding to the sustained reversal seen only in immobilized animals. FALL1 corresponds to the post-reversal ventral turn and FALL2 to the dorsal turn. FALL1 and FALL2, in conjunction with LOW, correspond to forward crawling. Slowing mapped to final sections of LOW

### Figure 3. SMDV Signals during Ventral, but Not Dorsal, Post-Reversal Turns

(A) Fractional histogram showing postural angle of first post-reversal head bend (ventral, yellow; dorsal, orange). Numbers indicate percentage of all post reversal head bends. Dashed vertical black line shows median of all other head bends (no difference between ventral and dorsal).

(B–E) SMDV  $Ca^{2+}$  imaging in freely moving animals.

(B) Example trace showing SMDV activity as normalized GCaMP/mCherry fluorescence ratio (black) and corresponding head-bend angle (purple). Pink bars overlay reverse crawling; yellow and orange bars overlay ventral and dorsal post-reversal head-bends, respectively.

(C and D) Average SMDV  $Ca^{2+}$  signals triggered to reversals ending with ventral (C) or dorsal (D) head bends. Upper and lower traces represent 90<sup>th</sup> and 10<sup>th</sup> percentile of all data, respectively. Number of recorded worms and events are indicated.

(E) Regression analysis of normalized peak post-reversal head-bend angle versus SMDV  $Ca^{2+}$  signal. Ventral and dorsal bends are shown in yellow and orange, respectively. Black open circles show an equal number of randomly

preceding RISEs (Figures 4B–4E, see [Experimental Procedures](#) for the detailed mapping rules). Thus, the neural state manifold, on a single trial basis, embeds the pirouette command sequence described in the state transition diagram (Figures 2A–2E). The neural trajectory follows the same unidirectional sequence through manifold sub-regions as the corresponding behavioral sequence executed by freely moving worms during pirouettes. This observation motivated us to redraw the state transition diagram (Figure 2E) as a continuous flow graph (Figure 4E). The neuronal manifold, in addition to embedding the command sequence, also contains information about graded locomotion parameters like the drive underlying crawling speed (Figure 4F, see [Experimental Procedures](#) for the detailed mapping rules). Both motor command states, as well as speed drive, appear organized on the manifold; i.e., separable sub-regions unambiguously delimit the distinct command states (Figure 4B) and proximal traversals on the manifold exhibit similar speed drives (Figure 4F). This manifold organization was clearly apparent in all five recordings (Figure S2E).

Each branching region of the manifold represents a decision where the subsequent motor state is determined. To explore the process of decision execution, we quantified the time course of trajectory separation when branching into RISE1 versus RISE2 and FALL1 versus FALL2 and subsequent merging. This approach calculates how significantly trajectory segments bundle in PCA space when tested against random shuffling of membership in RISE1 versus RISE2 or FALL1 versus FALL2 clusters (see [Supplemental Experimental Procedures](#) for details). Consistent with the significant clustering of neuronal recruitment vectors described above, there was significant separation during the RISE and FALL phases (Figures 4G and 4H). Interestingly, this also uncovered memory effects: a RISE1 versus RISE2 branch choice could, on average, be predicted during the preceding FALL period (Figure 4G), and consistent with the previous, FALL1 versus FALL2 trajectories remained significantly unmixed in the following RISE phases (Figure 4H). Moreover, RISE1 and RISE2 are associated, respectively, with long and short preceding LOW states (Figure 4I). Both results indicate that the trajectory path history influences the future branch choice decision.

In contrast to the state transition diagram, the neural state manifold captures the continuous dynamical structure of motor commands and their transitions and contains additional information about graded metrics of motion, like crawling speed and postural flexure. Here, we define the terms command state and speed drive as the brain's internal high-level representations of the underlying motor programs, since these are readily observable in immobilized animals in the absence of motor execution.

### Neural State Dynamics Persist When a Hub Output Neuron Is Inhibited

The presence of a representation of the pirouette sequence in immobilized animals suggests that the neuronal population dynamics are primarily internally driven and thus represent descending motor commands that can operate in the absence of motor feedback. We sought to further test this hypothesis. Despite the largely recurrent connectivity of the *C. elegans* wiring diagram, a bottleneck exists from the head ganglia to body motor neurons—AVA pre-motor interneurons are anatomical

network hubs linking head ganglia neurons to A-class ventral cord motor neurons, which mediate the reversal motor program (Chalfie et al., 1985; Kawano et al., 2011; Varshney et al., 2011). Acutely silencing AVA via transgenic expression of a histamine-gated chloride channel (HisCl) (Pokala et al., 2014) abolished reversals in freely moving worms (Figure 5A). As expected, similarly silenced animals under whole-brain imaging ( $n = 5$  recordings) showed substantial attenuation of AVA activity and strong uncoupling of AVA from the global brain cycle (Figures 5B and S6A). Additionally, activity of the reverse interneurons AVE and RIM, which are connected to AVA via gap junctions (White et al., 1986) was slightly attenuated (Figure 5B). However, their phase relationships with most other neurons appeared normal (Figure S6C). A-class ventral cord motor neurons, the principal output targets of AVA, also showed significant attenuation (Figure 5B). Despite these effects, the cyclical dynamics and neuronal recruitment patterns were largely preserved (Figures 5C, 5D, and S6). The distributions of network state durations were unchanged, with the exception of a decrease in HIGH state duration, suggesting that network HIGH state prolongation was due in part to reinforcement from AVA (Figure 5E). These observations raised the possibility that the global brain cycle was also intact in freely moving worms with AVA, and therefore reversals, inhibited. Unlike in wild-type animals, where 92.5% of turns occurred in conjunction with a preceding reversal, in worms with silenced AVA neurons, none of the turns were preceded by reversals; instead, 68% of turns (32 out of 47) were preceded by prolonged slowing or pauses, while the rest occurred during apparently normal forward locomotion. Imaging RIM in AVA-silenced freely moving animals revealed the presence of sustained RIM activity during these prolonged slowing or pauses preceding normal turning events (Figures 5F–5H). Such transients were never seen in controls, where RIM was only active during reversals. In AVA-silenced animals, RIM activity often entered HIGH states during prolonged pauses, further supporting the above interpretation that the HIGH state occurs due to the absence of effectual motor execution (Figures 5F and S3U–S3X). These results show that the cyclical time course of the brain-wide motor command is maintained in the absence of reversal execution, the only effect of which is a prolonged HIGH state duration. Analogously, behaviors that are not AVA-output mediated (slowing and turns) are also preserved. Further, these data imply that AVA is not a privileged generator of motor commands but should instead be characterized as an output-facing member of the collectively oscillating interneuron group.

### Entrainment of the Global Brain Cycle by Sensory Stimulation

Next, we investigated how these collective network dynamics interact with a chemosensory input. Under whole-brain imaging, we stimulated oxygen chemosensory neurons with consecutive oxygen up- and down-shifts (21% versus 4%), a protocol previously shown to reliably activate BAG, URX, and AQR oxygen sensory neurons and to entrain pirouette behavior with high pirouette probability at 21% oxygen and low at 4% (Figures S7A and S7B; see also references Busch et al., 2012; Schrödel et al., 2013; Zimmer et al., 2009). To our surprise, with the exception of one ventral ganglion neuron class (RIG or RIF)

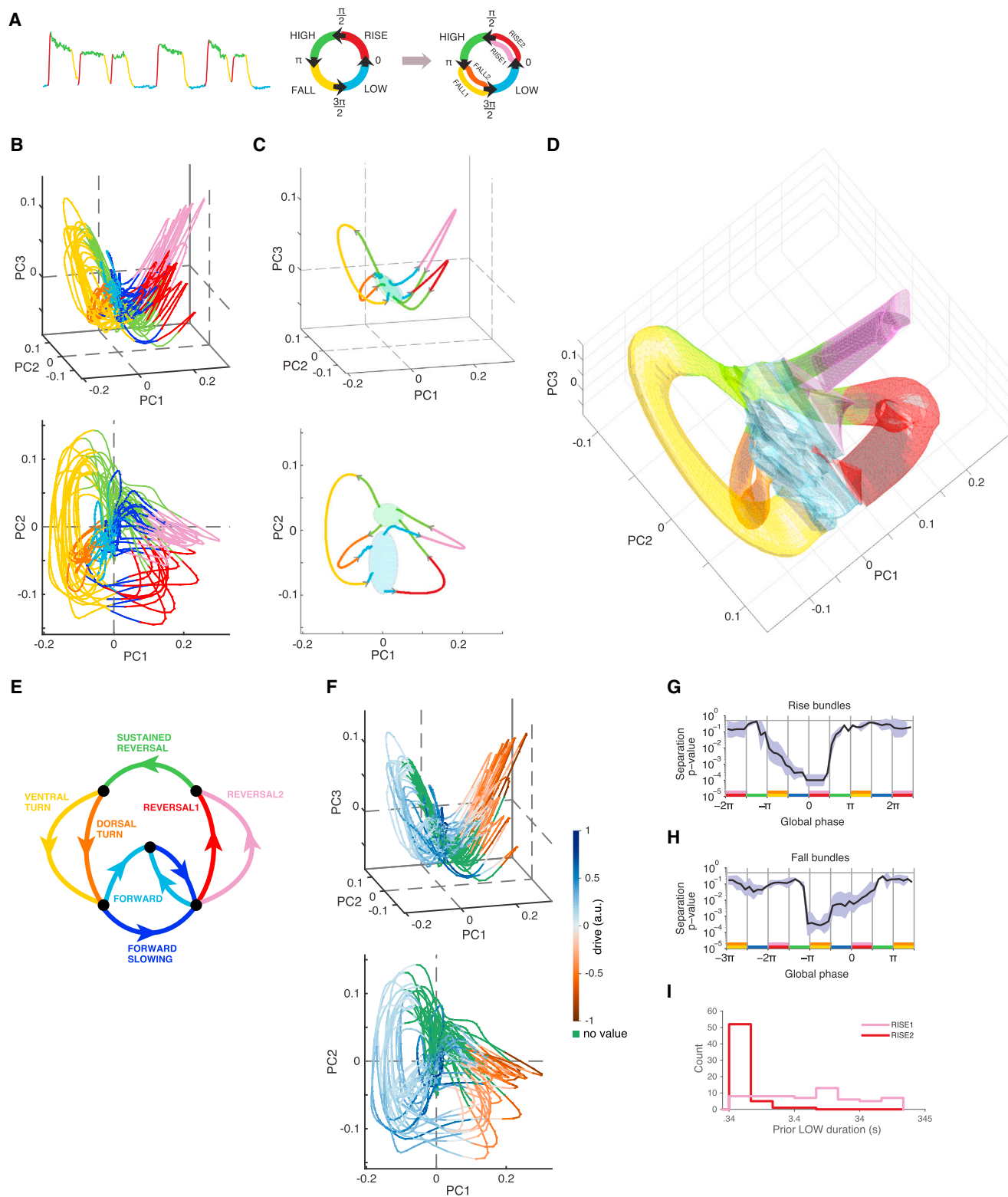


**Figure 4. The Neural State Manifold Embeds the Action Sequence and Exhibits Organized Analog Speed Drive**

(A) Phase segmentation of example AVAL trace (left). Four-state brain cycle (middle). Phase timing analysis and clustering leads to six-state brain cycle (right). See also Figures S4 and S5.

(B) Phase plot of the same trial shown in Figure 1, colored by six-state brain cycle plus FORWARD SLOWING command state in purple (see below).

(legend continued on next page)

(Figure S7C), we did not detect single-neuron representations of sensory stimulus downstream of sensory neurons ( $n = 13$  recordings). Moreover, the topology of the neural state manifold did not change upon stimulation; however, there were some magnitude effects on the amplitude of temporal PC1 (Figure 6A). Based on the strong entrainment effect the stimulation protocol has on pirouette behavior, we expected that oxygen concentration should affect bundle occupancy on the manifold. Indeed, the stimulus protocol entrained the global phase of the brain cycle so that the probability of the reverse motor command state declined during 4% oxygen periods and increased during 21% oxygen periods (Figures 6B and 6C), indicating a successful sensorimotor transformation in our preparation. Consistent with these findings,  $\text{Ca}^{2+}$  rises in BAG neurons during the HIGH state evoked immediate FALL1 or FALL2 transitions in 56% (30/54,  $n = 13$  recordings) of all instances (see Figure S7C for an example). Interestingly, in 22 out of the 24 remaining instances, secondary BAG  $\text{Ca}^{2+}$ -rises coincided with a FALL1 or FALL2 transition; these were the only times when we observed secondary BAG transients (see Figure S7C as an example). This finding suggests the existence of a feedback mechanism eliciting or gating secondary  $\text{Ca}^{2+}$  rises in the BAG sensory neurons, demonstrating that variability in the BAG sensory response profile (Zimmer et al., 2009) can be explained when the underlying brain state is known to the observer.

Finally, we looked for sensory-evoked  $\text{Ca}^{2+}$  activity in the major PC1 neuron classes AVA, AVE, and RIB in freely moving animals. Together AVE and RIB receive 47% of BAG neuron synapses (White et al., 1986). Consistent with our whole-brain imaging results, these neurons retained a tight correlation with motor state and movement metrics and lacked obvious sensory encoding activity; the magnitude of  $\text{Ca}^{2+}$  signals was subtly modulated during the stimulation periods (Figures S7D–S7U).

In summary, neural state manifold organization is robust to a salient sensory input and thus stably encodes the motor command sequences of the worm under these conditions. The major effect of sensory input was to modulate the probability that the neural state resides on a particular segment bundle by driving the neural state along a lawful trajectory. The result is an entrainment of the global brain cycle, which is consistent with the entrainment of corresponding motor behaviors in freely moving worms.

## DISCUSSION

In this work, we identify and characterize a brain-wide signal in *C. elegans* that dominates the neural activity time series.

Although our approach required the use of a nuclear localized  $\text{Ca}^{2+}$  indicator, omitting the detection of subcellular  $\text{Ca}^{2+}$  signals (Chalasan et al., 2007; Hendricks et al., 2012; Li et al., 2014), it reveals a pervasive motor state representation that is shared among most interneuron and motor neuron layers. The neural state trajectory exhibits directional, cyclical flow (Figure 1F) confined to a low-dimensional manifold (Figure 4D), organized into bundles (Figures 4B–4D) composed of stereotyped and smoothly changing neural activity vectors (Figure S5). Each motor command within the pirouette action sequence is reliably represented across several neurons. Neurons additionally encode graded parameters of locomotion, e.g., crawling speed and postural flexure (Figures 2, 3, and S3). These data enable us to unambiguously map behavioral commands onto sub-regions of the neural state manifold, enabling instantaneous behavioral decoding throughout an experimental trial (Figures 4B and 4E). We interpret these dynamics as corresponding to motor commands, as they can be decoupled from motor output either by restraint (during whole-brain imaging) or manipulation of a major output neuron (Figure 5). Organized flow along the neural state manifold mediates the assembly of motor commands into action sequences (Figures 4B and 4E); it thus represents the high-level temporal organization of behavior upstream of the generation of the animal's undulatory gait. This contrasts with population dynamics in the motor ganglia of crustaceans, mollusks, and lamprays that generate peristaltic and movement rhythms (Bruno et al., 2015; Grillner, 2006; Marder and Bucher, 2007). Interestingly, the brain's forward and reversal motor commands are coupled to corresponding rise, high, fall, and low states in the B- and A-class ventral nerve cord (VNC) motor neurons (Figures 1 and S1), which is consistent with previous studies performed in moving *C. elegans*. Additionally, VNC motor neuron activity exhibits gait-related rhythmic activity superimposed on these command states (Kawano et al., 2011; Wen et al., 2012), which requires proprioceptive coupling to movement (Wen et al., 2012). Taken together, we propose that behavioral state is encoded in the brain and coupled to the motor periphery and that this coupling co-occurs with locally maintained rhythmic activity.

These continuous neural dynamics embed behavioral motifs, described by the state transition diagram, and permit their superposition with graded motion metrics (Figure 4F). The process of decision making leading to execution of alternate behaviors can be observed as the time evolution of neural trajectories before the branches (Figures 4B–4D, 4G, and 4H). We propose that the phenomenon of global dynamics robustly and continuously encoding action sequence commands may be present in

(C) Phase-registered averages of the two RISE phase and two FALL phase bundles colored by six-state brain cycle. Semi-transparent ovals denote trajectory bundle mixing regions.

(D) Contour surface illustrating the neural state manifold colored by six-state brain cycle.

(E) Flow diagram indicating the motor command states corresponding to the six-state brain cycle plus FORWARD SLOWING command state (purple).

(F) The same phase plot colored by forward- and reverse-speed drive inferred from neural correlate decoding. Green trajectory segments indicate the SUSTAINED REVERSAL state, for which no drive correspondence is made. See Figure S2 for more examples.

(G and H) Quantification of inter-bundle separation and mixing for RISE (G) and FALL (H) clusters. Traces show trial-averaged p values (shading indicates SEM;  $n = 5$  animals) of mean normalized pairwise distance at instantaneous points in the past or future, which indicate the probability that the observed separation between bundles occurred by chance. This calculation was done in six dimensions (PC1–3 plus their derivatives) to incorporate directional information from the trajectory paths.

(I) Distribution of LOW state durations preceding RISE1 or RISE2 segments.

See also Movies S2 and S3.

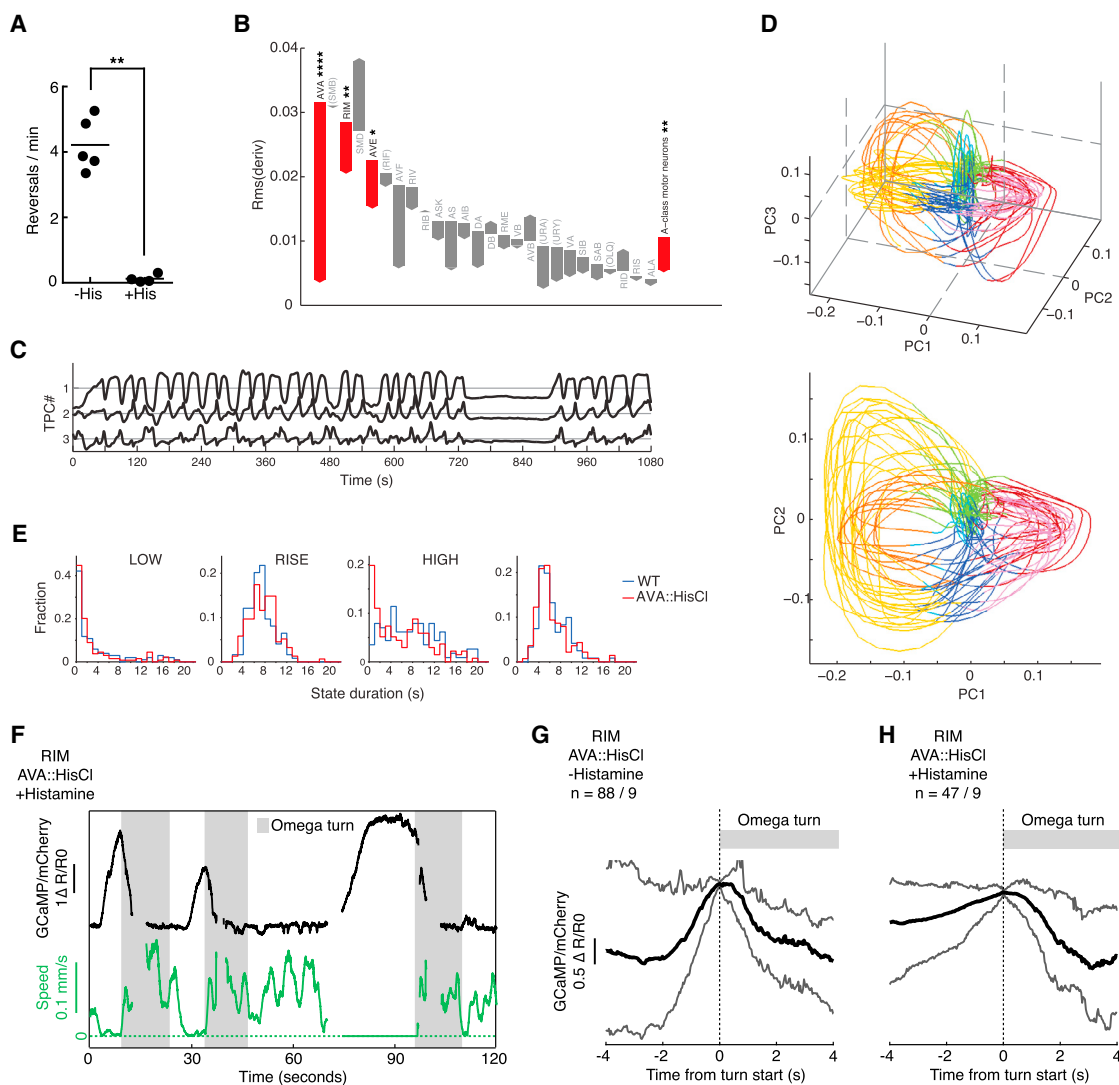


**Figure 5. Global Brain Dynamics Persist when Decoupled from Motor Output**

(A) Reversal events per minute for AVA::HisCl worms without (–His) or with (+His) histamine treatment. Each data point represents a single assay,  $n = 20$ – $25$  worms per assay. Horizontal lines show means. Mann-Whitney test,  $**p < 0.01$ .

(B) Shifts in trial-averaged root-mean-squared power of neuronal trace derivatives of AVA::HisCl worms with histamine treatment, relative to wild-type control ( $n = 5$ ). Gray bars indicate non-significant power shifts, red bars indicate significant power shifts. Class-A motor neurons, typically 1–2 visible per recording, were combined. Significance was determined using a permutation test,  $****p < 0.0001$ ,  $**p < 0.01$ ,  $*p < 0.05$ .

(C and D) Integrated temporal PCs (C) and phase plots (D) of an example AVA::HisCl dataset.

(E) Distributions of state durations of AVA::HisCl (red) versus wild-type (blue) across multiple trials ( $n = 5$ ).

(F–H)  $Ca^{2+}$  imaging of RIM in freely moving animals expressing HisCl in AVA.

(F) Example trace showing RIM activity in an AVA::HisCl worm after histamine treatment. Normalized GCaMP/mCherry fluorescence ratio (black) and corresponding crawling speed (green) are shown. Omega turns are indicated with gray overlaid bars. These worms did not exhibit reversals.

(G and H) Averages of RIM  $Ca^{2+}$  signals in AVA::HisCl worms triggered to omega turn onset, for worms pre-incubated without (G) or with (H) histamine. Upper and lower traces represent 90<sup>th</sup> and 10<sup>th</sup> percentile of all data, respectively. Number of recorded worms and omega turns are indicated.

See also Figure S6.

higher animals with more sophisticated behavioral repertoires. This hypothesis is supported by the observation of smooth population dynamics maintaining navigational plans in rodents (Harvey et al., 2012). Its generality could be further tested by studying the basis of well-described sequential courtship and grooming behaviors in fruit flies (Dankert et al., 2009; Seeds et al., 2014).

The ability to find dynamical structure solely on the basis of neural event timing (Figure S5) suggests that the structure we observe is not a particular consequence of the graded, non-spiking, nature of *C. elegans* neurons. We speculate that neuronal population trajectories associated with action selection in leeches (Brigman et al., 2005), limb movement in monkey

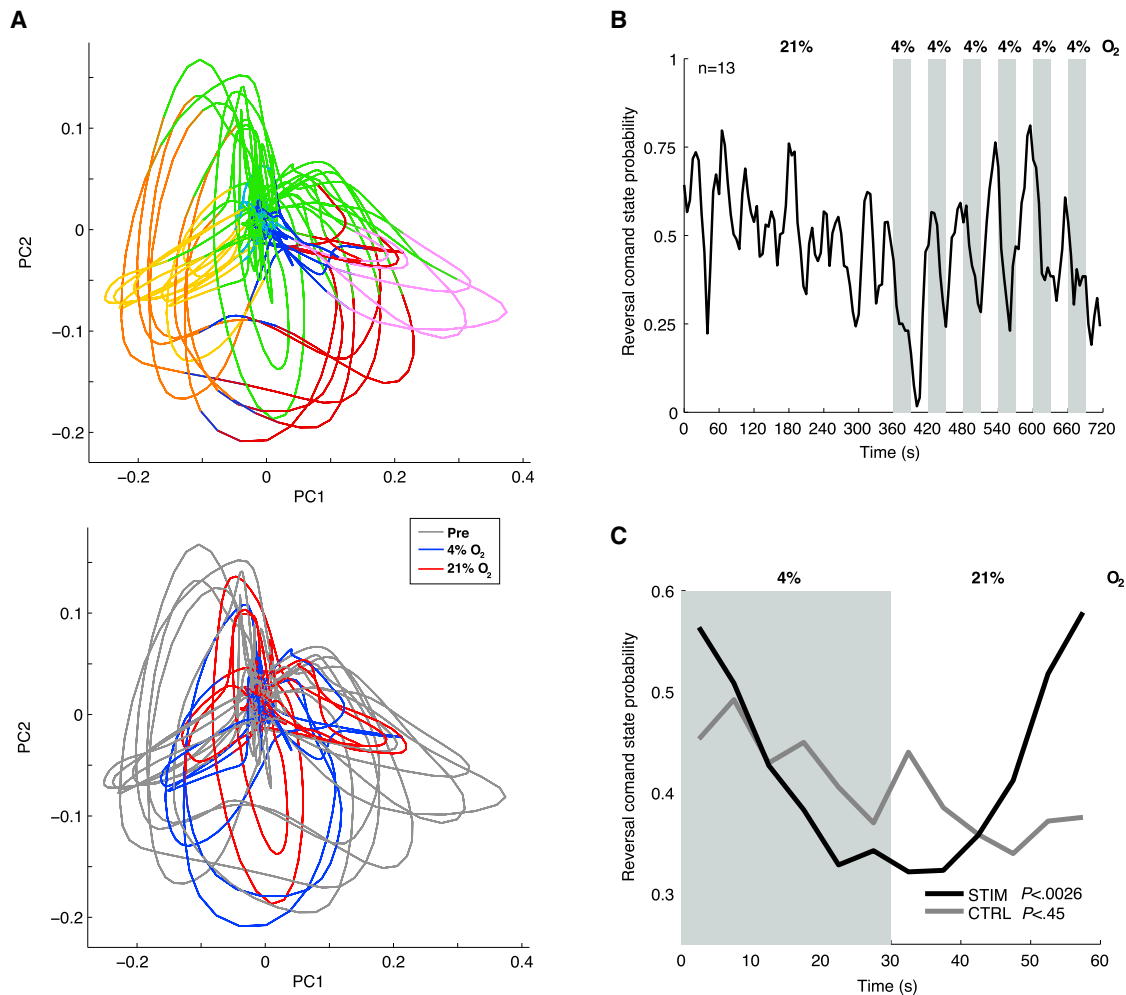


**Figure 6. Entrainment of the Global Brain Cycle by Sensory Stimulation**

Animals were recorded and stimulated with the oxygen profile indicated in (B).

(A) Phase plots of temporal PCs 1–2 from a representative recording. Top: behavioral command state coloring as in Figure 4B. Bottom: trajectory segments during the pre-stimulus period are labeled gray; segments during the 4% and 21% shift periods are labeled blue and red, respectively.

(B) The trace shows the probability of reversal command state (REVERSAL1 + REVERSAL2 + SUSTAINED REVERSAL) calculated over  $n = 13$  recordings.

(C) Reversal command state probability as in (B) but averaged over the six down- and up-shift periods.  $p$  values are calculated by a resampling test and indicate the probability that the stimulus-synced profile shape occurred from a randomly time-shifted stimulus pattern.

See also Figure S7.

cortical areas (Georgopoulos and Carpenter, 2015; Shenoy et al., 2013), and speech in humans (Bouchard et al., 2013) may be sparsely sampled windows onto similarly well-organized, smooth global dynamics.

Our work establishes a framework for future studies aimed at embedding more fine-scaled behaviors beyond the discrete classifications of the state transition diagram, such as gradual steering commands (Iino and Yoshida, 2009) and locomotory gait (Stephens et al., 2008). By exploring more sophisticated sensory input paradigms and studying the animal in different contexts and life stages, we expect that the neural state manifold will be further sub-dividable and support the mapping of other behavioral parameters. Additionally, in-depth analysis of whole-brain activity may uncover previously hidden

aspects of behavior; for example, we found two types of reversals (corresponding to RISE1 and RISE2) in whole-brain activity that currently lack known behavioral correlates. Although AVA inhibition had only subtle effects, systematically expanding this approach to other neurons and combinations thereof should reveal whether individual neurons or sub-ensembles are causal to brain dynamics. By probing the system with acute perturbation using optogenetics and imaging at finer timescales and sub-neuronal spatial resolution, it should be possible to uncover the neuronal logic governing trajectory control and branch selection, which underlies decision making in this system. Measuring manifold geometry changes over longer timescales may uncover the characteristics of brain states such as hunger-satiety or sleep-wakefulness.

Our results argue against models of largely feed-forward sensory-to-motor flow where intermediate neuronal layers perform sequential processing and the behavioral state is only ultimately represented within the nervous system at the motor periphery. Instead, our data support a model of an early interface between sensory and motor representations as was suggested by recent single-neuron studies (Hendricks et al., 2012; Luo et al., 2014).

Moreover, motor command representations affect responsiveness of sensory neurons and early interneurons to sensory inputs via feedback mechanisms (Figure S7) that remain to be identified (see also Gordus et al., 2015). Consistent with recent distributed models of sensorimotor action selection in mammals, including primates (Cisek and Kalaska, 2010), our work suggests that the brain's outputs—i.e., its intents and actions—make up a large fraction of its dynamic activity state.

Our findings reveal that a large collection of neuronal classes with distinct morphologies and connectivities (White et al., 1986), distinct molecular compositions and neurotransmitter expression patterns (Hobert, 2013), distinct synaptic transmission properties (Li et al., 2014), and distinct subcellular signal processing capacities (Chalasan et al., 2007; Hendricks et al., 2012; Li et al., 2014) nevertheless collectively share a low-dimensional, pervasive neuronal signal. The class-specific phase relationships with respect to the global brain cycle (Figures S1B and S5) suggest that neurons differentially interact with this shared mode. We therefore propose that the neural state manifold influences and binds local activity to a global reference framework, establishing a consensus that produces stable, coherent behavior.

## EXPERIMENTAL PROCEDURES

The Supplemental Experimental Procedures contain more detailed information on each procedure, and in addition, they include descriptions of region of interest detection and neural time series extraction from volumetric  $\text{Ca}^{2+}$  imaging data, electrophysiology, simulation of nuclear GCaMP signals from voltage traces, population behavior assays, statistics applied in this study, strain genotypes, and molecular biology constructs.

### Whole-Brain $\text{Ca}^{2+}$ Imaging of *C. elegans* Head Ganglia Neurons

Animals were immobilized with 1 mM tetramisole in microfluidic devices that allow controlled  $\text{O}_2$  stimuli as previously described (Schröder et al., 2013; Zimmer et al., 2009). Recordings were started within 5 min after removal from food. Worms were either imaged for 18 min at constant 21%  $\text{O}_2$  or, for the stimulus protocol, imaged for 12 min with the first 6 min at 21%  $\text{O}_2$  and the remaining 6 min with 30 s consecutive shifts between 4% and 21%  $\text{O}_2$ . Data were acquired using an inverted spinning disc microscope (UltraViewVoX, PerkinElmer) equipped with an EMCCD camera (C9100-13, Hamamatsu).

### Identification of Head Ganglia Neurons

In each recording, we detected 107–131 neurons, covering 55%–67% of expected neurons in the imaging area. Neurons were identified taking into account their anatomical positions, also in relation to surrounding neurons (<http://www.wormatlas.org>), and their activity patterns. To confirm ambiguous neuron identities, marker lines expressing red fluorophores in neurons of interest were generated and crossed to the imaging line expressing GCaMP5K pan-neuronally in the nucleus (ZIM504).

### Time Series Analysis: PCA, Numerical Differentiation, 4-Phase Segmentation, Phase Timing Analysis, and Clustering

PCA was performed on the time derivatives of  $\Delta F/F_0$  neural traces, each normalized by its peak magnitude. To compute de-noised time derivatives

without the need of smoothing that can affect precise timing of sharp transitions, the total-variation regularization method (Chartrand, 2011) was applied. To segment individual neuronal activity into 4-phase sequences, first RISE and FALL phases for neurons were identified as periods when the time derivative was greater or lower than a small threshold, respectively. HIGH and LOW phases were then inferred in the remaining gaps. For trajectory segment averaging (Figures 4C, 4D, and S2E) and generation of Movies S2 and S3, neuronal time series were registered to a common phase clock by matching phase segment starts and ends to the reference neuron (AVA or RIM) rise onsets and fall offsets, respectively, followed by linearly interpolating within phase segments. To perform phase timing analysis, first a set of global transitions, either RISE or FALL onsets, were defined by the transitions of a reference neuron (AVA or RIM in this study). Then, relative time delays of the nearest transitions found in other neurons were used to compose a feature vector for each global transition. In the absence of a matching transition within 7 s of the reference neuron transition, a time delay of  $-10$  s was used for the purposes of clustering, since the absence of neurons was also considered an important feature of transitions. *K*-means clustering was applied to transition feature vectors for each full trial using  $L_1$  distance and  $k = 2$ . Detailed explanations of the above computational analyses may be found in the Supplemental Experimental Procedures.

### Behavioral Decoding of Whole-Brain Recordings

Each time point of the phase plot trajectory was first assigned to a global brain cycle HIGH, LOW, RISE1, RISE2, FALL1, or FALL2 segment as described above and in the main text, then mapped to motor command states as follows. RISE1 and RISE 2 segments were mapped to REVERSAL1 and REVERSAL2 command states, respectively. HIGH segments were mapped to the SUSTAINED REVERSAL state. FALL1 and FALL2 segments were mapped to VENTRAL TURN and DORSAL TURN, respectively. LOW segments were mapped to FORWARD except that RIB FALL phases present during global LOW segments were mapped to FORWARD SLOWING command states. A speed drive was assigned to each point on the trajectory as follows, aside from those in SUSTAINED REVERSAL phases for which no speed drive was inferred. During VENTRAL TURN, DORSAL TURN, FORWARD, and FORWARD SLOWING phases, positive speed drive was taken to be the magnitude of RIB activity, normalized to its most negative value during the trial. During REVERSAL1 and 2 phases, negative speed drive was taken to be the derivative of RIM neuron activity, normalized to its highest value during the trial.

### $\text{Ca}^{2+}$ Imaging in Freely Moving Animals

$\text{Ca}^{2+}$  imaging recordings were made using the automatic re-centering system described previously (Faumont et al., 2011) with custom modifications. Young adult worms (0–8 eggs) expressed both mCherry and GCaMP in the neuron of interest. Animals were recorded while freely crawling on agar in a custom built microscope stage containing an airtight chamber with inlet and outlet connectors for gas flow delivery. Images were acquired using two CCD cameras (Evolve 512, Photometrics) connected via a DualCam DC2 beam splitter (Photometrics). A long-distance 63 $\times$  objective (Zeiss LD Plan-Neofluar 63 $\times$ , 0.75 NA) was used to obtain unbinned images streamed at 30.3 frames per second (fps) acquisition rate. Simultaneous behavior recordings under infrared illumination (780 nm) were made using a CCD camera (Manta Prosilica GigE, Applied Vision Technologies) at 4 $\times$  magnification and 10 fps acquisition rate.

## SUPPLEMENTAL INFORMATION

Supplemental Information includes Supplemental Experimental Procedures, seven figures, one table, and three movies and can be found with this article online at <http://dx.doi.org/10.1016/j.cell.2015.09.034>.

## AUTHOR CONTRIBUTIONS

S.K. designed experiments, developed analytical methods for whole-brain imaging datasets, and analyzed data. H.S.K. designed experiments, generated transgenic strains, performed  $\text{Ca}^{2+}$ -imaging experiments in freely moving animals, developed analytical methods, and analyzed data. T.S. designed

experiments, generated transgenic strains, performed whole-brain imaging experiments, and analyzed data. S.S. performed population behavioral recordings and analyzed data. T.H.L. and S.L. performed electrical recordings; E.Y. wrote code for behavioral analysis; and M.Z. designed experiments, developed analytical methods, and led the project. S.K., H.S.K., T.S., and M.Z. wrote the manuscript.

## ACKNOWLEDGMENTS

We thank Cori Bargmann, Larry Abbott, Alipasha Vaziri, Andrew Straw, Hagai Lalazar, Omri Barak, and Sean Escola for critically reading the manuscript, Richard Latham for technical support, and Martin Colombini for manufacturing of mechanical components. The research leading to these results has received funding from the European Community's Seventh Framework Programme (FP7/2007-2013)/ERC grant agreement number 281869 (acronym: *elegans Neurocircuits*) to M.Z., the Simons Foundation (grant number 324958 to M.Z.), an EMBO Long Term Fellowship to S.K. (number ALTF 345-2014), an NIH training grant to T.H.L. (number F31 NS061697), an NIH T32 training grant to E.Y. (number T32 MH015174-38), and the Research Institute of Molecular Pathology (IMP). The IMP is funded by Boehringer Ingelheim.

Received: July 2, 2015

Revised: August 14, 2015

Accepted: September 2, 2015

Published: October 15, 2015

## REFERENCES

- Ahrens, M.B., Li, J.M., Orger, M.B., Robson, D.N., Schier, A.F., Engert, F., and Portugues, R. (2012). Brain-wide neuronal dynamics during motor adaptation in zebrafish. *Nature* **485**, 471–477.
- Ahrens, M.B., Orger, M.B., Robson, D.N., Li, J.M., and Keller, P.J. (2013). Whole-brain functional imaging at cellular resolution using light-sheet microscopy. *Nat. Methods* **10**, 413–420.
- Anderson, D.J., and Perona, P. (2014). Toward a science of computational ethology. *Neuron* **84**, 18–31.
- Bouchard, K.E., Mesgarani, N., Johnson, K., and Chang, E.F. (2013). Functional organization of human sensorimotor cortex for speech articulation. *Nature* **495**, 327–332.
- Briggman, K.L., Abarbanel, H.D., and Kristan, W.B., Jr. (2005). Optical imaging of neuronal populations during decision-making. *Science* **307**, 896–901.
- Bruno, A.M., Frost, W.N., and Humphries, M.D. (2015). Modular deconstruction reveals the dynamical and physical building blocks of a locomotion motor program. *Neuron* **86**, 304–318.
- Busch, K.E., Laurent, P., Soltesz, Z., Murphy, R.J., Favre, O., Hedwig, B., Thomas, M., Smith, H.L., and de Bono, M. (2012). Tonic signaling from O<sub>2</sub> sensors sets neural circuit activity and behavioral state. *Nat. Neurosci.* **15**, 581–591.
- Chalasan, S.H., Chronis, N., Tsunozaki, M., Gray, J.M., Ramot, D., Goodman, M.B., and Bargmann, C.I. (2007). Dissecting a circuit for olfactory behaviour in *Caenorhabditis elegans*. *Nature* **450**, 63–70.
- Chalfie, M., Sulston, J.E., White, J.G., Southgate, E., Thomson, J.N., and Brenner, S. (1985). The neural circuit for touch sensitivity in *Caenorhabditis elegans*. *J. Neurosci.* **5**, 956–964.
- Chartrand, R. (2011). Numerical differentiation of noisy, nonsmooth data. *ISRN Applied Mathematics* **2011**, 1–11.
- Churchland, M.M., Cunningham, J.P., Kaufman, M.T., Foster, J.D., Nuyujukian, P., Ryu, S.I., and Shenoy, K.V. (2012). Neural population dynamics during reaching. *Nature* **487**, 51–56.
- Cisek, P., and Kalaska, J.F. (2010). Neural mechanisms for interacting with a world full of action choices. *Annu. Rev. Neurosci.* **33**, 269–298.
- Cunningham, J.P., and Yu, B.M. (2014). Dimensionality reduction for large-scale neural recordings. *Nat. Neurosci.* **17**, 1500–1509.
- Dankert, H., Wang, L., Hoopfer, E.D., Anderson, D.J., and Perona, P. (2009). Automated monitoring and analysis of social behavior in *Drosophila*. *Nat. Methods* **6**, 297–303.
- Donnelly, J.L., Clark, C.M., Leifer, A.M., Pirri, J.K., Haburcak, M., Francis, M.M., Samuel, A.D.T., and Alkema, M.J. (2013). Monoaminergic orchestration of motor programs in a complex *C. elegans* behavior. *PLoS Biol.* **11**, e1001529.
- Faumont, S., Rondeau, G., Thiele, T.R., Lawton, K.J., McCormick, K.E., Sottile, M., Griesbeck, O., Heckscher, E.S., Roberts, W.M., Doe, C.Q., and Lockery, S.R. (2011). An image-free opto-mechanical system for creating virtual environments and imaging neuronal activity in freely moving *Caenorhabditis elegans*. *PLoS ONE* **6**, e24666.
- Georgopoulos, A.P., and Carpenter, A.F. (2015). Coding of movements in the motor cortex. *Curr. Opin. Neurobiol.* **33**, 34–39.
- Gordus, A., Pokala, N., Levy, S., Flavell, S.W., and Bargmann, C.I. (2015). Feedback from network states generates variability in a probabilistic olfactory circuit. *Cell* **161**, 215–227.
- Gray, J.M., Hill, J.J., and Bargmann, C.I. (2005). A circuit for navigation in *Caenorhabditis elegans*. *Proc. Natl. Acad. Sci. USA* **102**, 3184–3191.
- Grillner, S. (2006). Biological pattern generation: the cellular and computational logic of networks in motion. *Neuron* **52**, 751–766.
- Ha, H.I., Hendricks, M., Shen, Y., Gabel, C.V., Fang-Yen, C., Qin, Y., Colón-Ramos, D., Shen, K., Samuel, A.D.T., and Zhang, Y. (2010). Functional organization of a neural network for aversive olfactory learning in *Caenorhabditis elegans*. *Neuron* **68**, 1173–1186.
- Harvey, C.D., Coen, P., and Tank, D.W. (2012). Choice-specific sequences in parietal cortex during a virtual-navigation decision task. *Nature* **484**, 62–68.
- Hendricks, M., Ha, H., Maffey, N., and Zhang, Y. (2012). Compartmentalized calcium dynamics in a *C. elegans* interneuron encode head movement. *Nature* **487**, 99–103.
- Hobert, O. (2013). The neuronal genome of *Caenorhabditis elegans* (Worm-Book), pp. 1–106.
- Iino, Y., and Yoshida, K. (2009). Parallel use of two behavioral mechanisms for chemotaxis in *Caenorhabditis elegans*. *J. Neurosci.* **29**, 5370–5380.
- Jin, X., Tecuapetla, F., and Costa, R.M. (2014). Basal ganglia subcircuits distinctively encode the parsing and concatenation of action sequences. *Nat. Neurosci.* **17**, 423–430.
- Jolliffe, I.T. (2002). *Principal Component Analysis*, Second Edition (Springer).
- Kawano, T., Po, M.D., Gao, S., Leung, G., Ryu, W.S., and Zhen, M. (2011). An imbalancing act: gap junctions reduce the backward motor circuit activity to bias *C. elegans* for forward locomotion. *Neuron* **72**, 572–586.
- Kimata, T., Sasakura, H., Ohnishi, N., Nishio, N., and Mori, I. (2012). Thermo-taxis of *C. elegans* as a model for temperature perception, neural information processing and neural plasticity. *Worm* **1**, 31–41.
- Laurent, P., Soltesz, Z., Nelson, G.M., Chen, C., Arellano-Carbajal, F., Levy, E., and de Bono, M. (2015). Decoding a neural circuit controlling global animal state in *C. elegans*. *eLife* **4**, 4.
- Lemon, W.C., Pulver, S.R., Höckendorf, B., McDole, K., Branson, K., Freeman, J., and Keller, P.J. (2015). Whole-central nervous system functional imaging in larval *Drosophila*. *Nat. Commun.* **6**, 7924.
- Li, Z., Liu, J., Zheng, M., and Xu, X.Z.S. (2014). Encoding of both analog- and digital-like behavioral outputs by one *C. elegans* interneuron. *Cell* **159**, 751–765.
- Luo, L., Wen, Q., Ren, J., Hendricks, M., Gershow, M., Qin, Y., Greenwood, J., Soucy, E.R., Klein, M., Smith-Parker, H.K., et al. (2014). Dynamic encoding of perception, memory, and movement in a *C. elegans* chemotaxis circuit. *Neuron* **82**, 1115–1128.
- Mante, V., Sussillo, D., Shenoy, K.V., and Newsome, W.T. (2013). Context-dependent computation by recurrent dynamics in prefrontal cortex. *Nature* **503**, 1–19.
- Marder, E., and Bucher, D. (2007). Understanding circuit dynamics using the stomatogastric nervous system of lobsters and crabs. *Annu. Rev. Physiol.* **69**, 291–316.

- Panier, T., Romano, S.A., Olive, R., Pietri, T., Sumbre, G., Candelier, R., and Debrégeas, G. (2013). Fast functional imaging of multiple brain regions in intact zebrafish larvae using selective plane illumination microscopy. *Front. Neural Circuits* 7, 65.
- Pierce-Shimomura, J.T., Morse, T.M., and Lockery, S.R. (1999). The fundamental role of pirouettes in *Caenorhabditis elegans* chemotaxis. *J. Neurosci.* 19, 9557–9569.
- Pokala, N., Liu, Q., Gordus, A., and Bargmann, C.I. (2014). Inducible and titratable silencing of *Caenorhabditis elegans* neurons in vivo with histamine-gated chloride channels. *Proc. Natl. Acad. Sci. USA* 111, 2770–2775.
- Prevedel, R., Yoon, Y.-G., Hoffmann, M., Pak, N., Wetzstein, G., Kato, S., Schrödel, T., Raskar, R., Zimmer, M., Boyden, E.S., and Vaziri, A. (2014). Simultaneous whole-animal 3D imaging of neuronal activity using light-field microscopy. *Nat. Methods* 11, 727–730.
- Schrödel, T., Prevedel, R., Aumayr, K., Zimmer, M., and Vaziri, A. (2013). Brain-wide 3D imaging of neuronal activity in *Caenorhabditis elegans* with sculpted light. *Nat. Methods* 10, 1013–1020.
- Seeds, A.M., Ravbar, P., Chung, P., Hampel, S., Midgley, F.M., Jr., Mensh, B.D., and Simpson, J.H. (2014). A suppression hierarchy among competing motor programs drives sequential grooming in *Drosophila*. *eLife* 3, e02951.
- Shenoy, K.V., Sahani, M., and Churchland, M.M. (2013). Cortical control of arm movements: a dynamical systems perspective. *Annu. Rev. Neurosci.* 36, 337–359.
- Stephens, G.J., Johnson-Kerner, B., Bialek, W., and Ryu, W.S. (2008). Dimensionality and dynamics in the behavior of *C. elegans*. *PLoS Comput. Biol.* 4, e1000028.
- Varshney, L.R., Chen, B.L., Paniagua, E., Hall, D.H., and Chklovskii, D.B. (2011). Structural properties of the *Caenorhabditis elegans* neuronal network. *PLoS Comput. Biol.* 7, e1001066.
- Wen, Q., Po, M.D., Hulme, E., Chen, S., Liu, X., Kwok, S.W., Gershow, M., Leifer, A.M., Butler, V., Fang-Yen, C., et al. (2012). Proprioceptive coupling within motor neurons drives *C. elegans* forward locomotion. *Neuron* 76, 750–761.
- White, J.G., Southgate, E., Thomson, J.N., and Brenner, S. (1986). The structure of the nervous system of the nematode *Caenorhabditis elegans*. *Philos. Trans. R. Soc. Lond. B Biol. Sci.* 314, 1–340.
- Zimmer, M., Gray, J.M., Pokala, N., Chang, A.J., Karow, D.S., Marletta, M.A., Hudson, M.L., Morton, D.B., Chronis, N., and Bargmann, C.I. (2009). Neurons detect increases and decreases in oxygen levels using distinct guanylate cyclases. *Neuron* 61, 865–879.



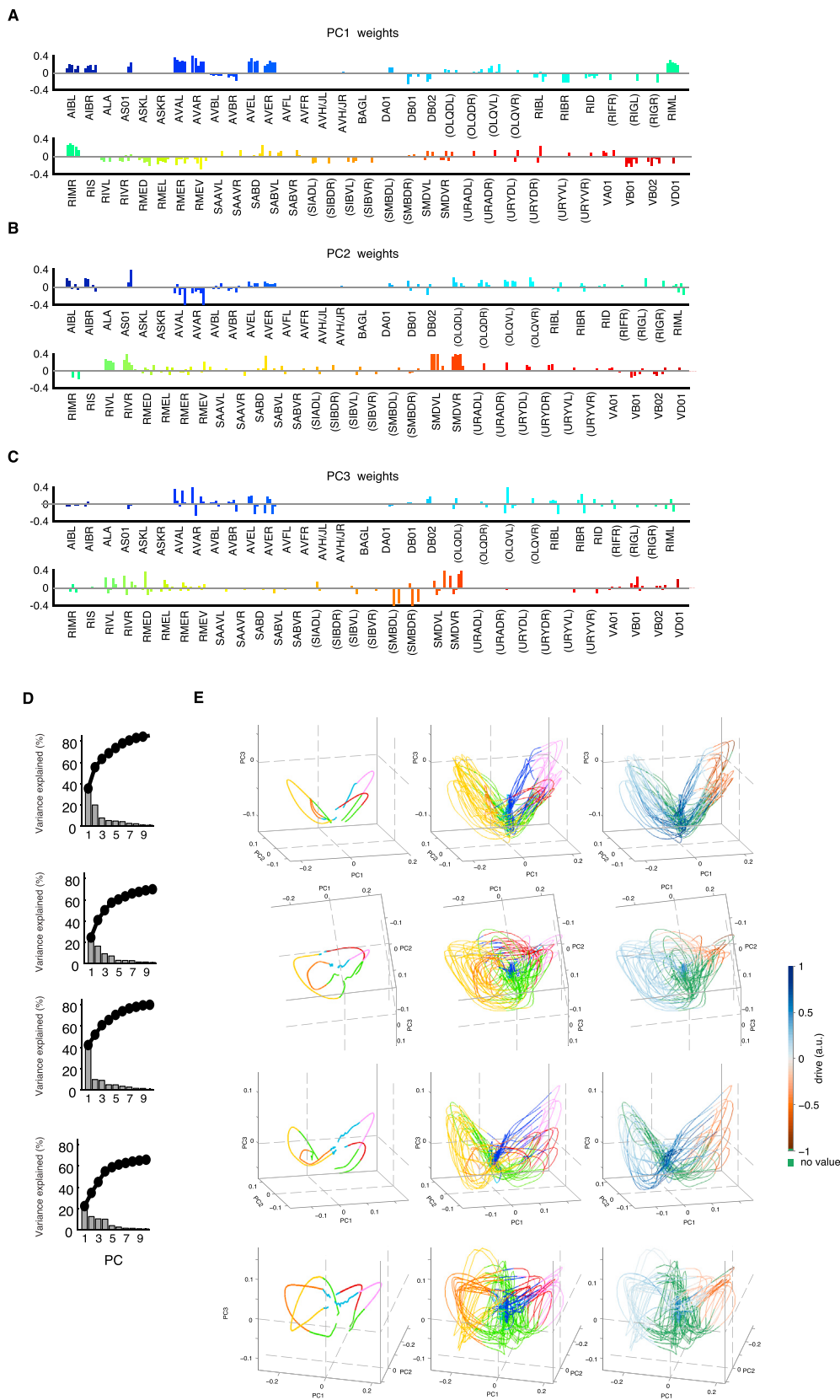
---

**Figure S1. Patterns of Neuronal Recruitment Map to Sub-regions of the Neural State Manifold, Related to Figure 1**

Data are from the same example recording shown in [Figure 1](#).

(A) Single traces of all recorded neurons colored and grouped by their maximum principal component weight (out of PC1–3) and sign as in [Figure 1](#).

(B) Each panel is a phase plot of the first two temporal PCs as in [Figure 1G](#). All panels are labeled by the  $\text{Ca}^{2+}$  rise (red balls) and fall (green balls) phases of the indicated neurons. Note that each neuron is recruited to a class-specific sub-region on the manifold. Ambiguous neuron IDs are shown in parentheses.



(legend on next page)

---

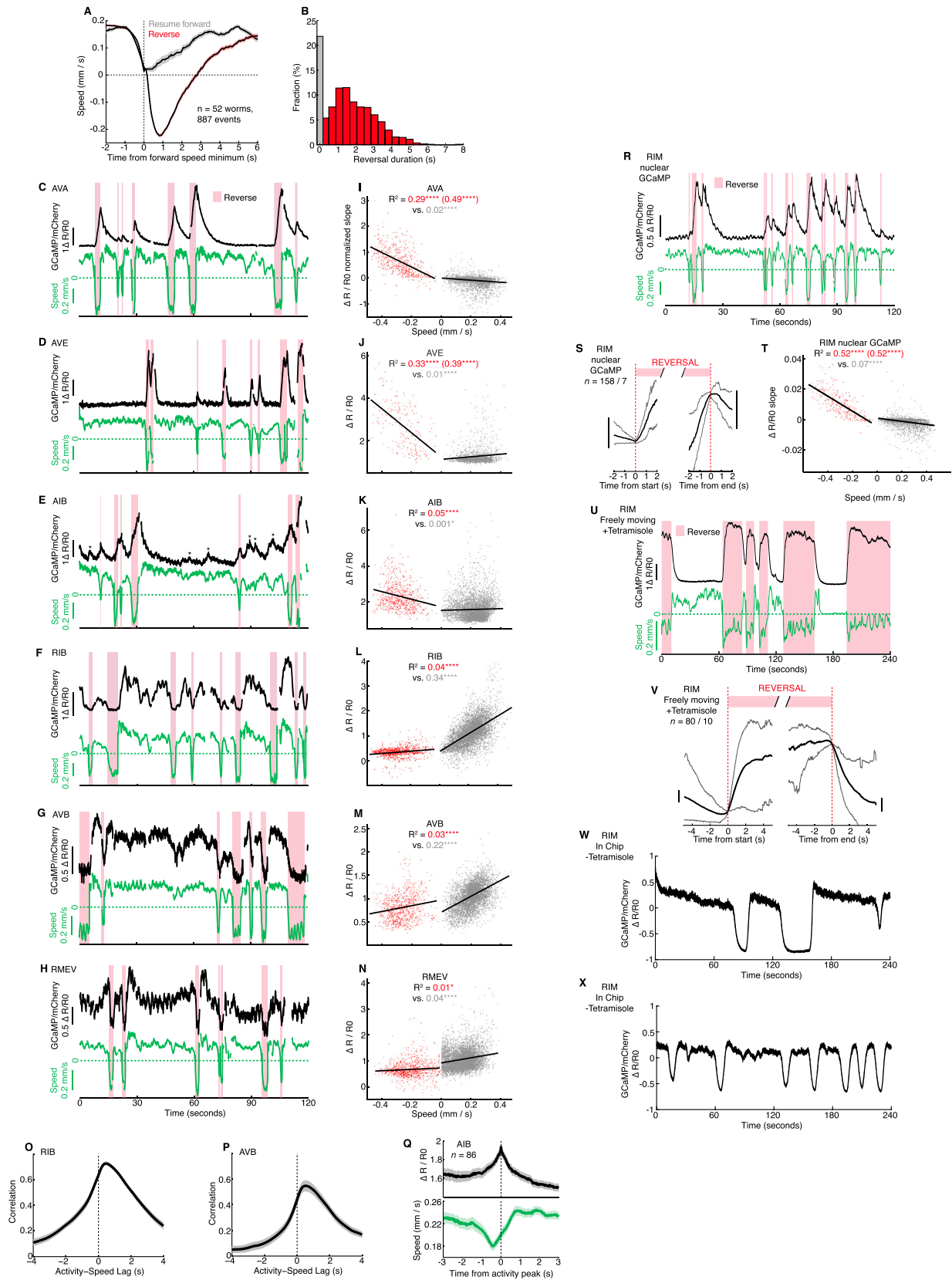
**Figure S2. Inter-trial Variability of PC1–3 Compositions and Manifold Structure, Related to Figure 1**

(A) PC1 coefficients for the 5 trials, grouped by neuron identity, and in order of trial.

(B and C) (B) PC2 coefficients, (C) PC3 coefficients. Not every neuron was identified in all 5 trials; blank values indicate that the neuron was not identified in that trial. Inter-trial regularity of coefficients show that the same neuron-specific dynamical features tend to dominate the global brain signal. Ambiguous neuron class IDs are in parentheses. Additional candidates: URA: URY; OLQ: URY; URY: OLQ; RIF: AVG/DD01; SMB: SMD/RMF; SIA: SIB; SIB: SIA; RIG: RIF/DB.

(D) Percentage variance explained for the 4 additional trials; same analysis as in Figure 1E.

(E) Repetitions of the state space trajectory analysis in Figures 4B, 4C, and 4F on the 4 additional animals included in all analysis. RISE/FALL bundle separations are visible. The orientation of the manifold relative to the PC2 and PC3 axes varied, so the camera viewpoint was rotated to visually match manifold geometry between trials.



(legend on next page)

**Figure S3. Several Interneurons Encode Motor State and Crawling Speed, and HIGH States Are Caused by Tetramisole or Confinement Alone, Related to Figures 2 and 4**

(A) Crawling speed during spontaneous slowing events. Traces show event-triggered average speed ( $\pm$ SEM) aligned to forward speed minimum before transition to reversal (red) or resumption of forward crawling (gray). Reversal speed is shown as negative.

(B) Fractional histogram of reversal duration after slowing events; 0 bin corresponds to no reversal.

(C–Q)  $\text{Ca}^{2+}$  imaging in freely moving animals (same recordings as in Figure 2H).

(C–H) Example traces showing the activities of indicated neurons by normalized GCaMP/mCherry fluorescence ratio (black) and corresponding crawling speed (green). Pink bars overlay reverse crawling periods. (C) AVA, co-recorded with RIM (Figure 2F). Synchronous activity between AVA and RIM was seen across 5 such co-recordings. (D) AVE. (E) AIB. (F) RIB. (G) AVB. (H) RMEV.

(I–N), Regression analysis of crawling speed versus normalized  $\text{Ca}^{2+}$  signal slope (I) or absolute  $\text{Ca}^{2+}$  signal (J–N) for the indicated neurons.  $R^2$  indicates goodness of fit for linear fits to reverse (red; parentheses indicate  $R^2$  for one maximum value for each individual reversal) and forward (gray) groups. Number of recordings is the same as in Figure 2H. Permutation test p-value: \*\*\*\*p < 0.0001 \*p < 0.05.

(O and P) Average cross-correlation ( $\pm$ SEM) between  $\text{Ca}^{2+}$ -signal and crawling speed during forward movement, for RIB (O) and AVB (P). Sharp drop in correlation magnitude from  $t = 0$  indicates that these neurons correlate with forward speed as it changes on the order of seconds.

(Q) Event-triggered averages of AIB activity ( $\pm$ SEM, upper panel) and crawling speed ( $\pm$ SEM, lower panel) aligned to activity peaks detected during forward movement, as shown by asterisks in (E).

(R–T) RIM  $\text{Ca}^{2+}$ -imaging recorded using nuclear-localized GCaMP.

(R) Example trace showing normalized GCaMP/mCherry fluorescence ratio (black) and corresponding crawling speed (green). Pink bars overlay reverse crawling periods.

(S) Event-triggered averages of  $\text{Ca}^{2+}$ -signals aligned to reversal onset (left) or reversal end (right). Number of recorded worms and events are indicated. Vertical line next to each trace indicates  $0.5 \Delta R/R_0$ . Compare to Figure 2H, top row.

(T) Regression analysis of crawling speed versus  $\text{Ca}^{2+}$ -signal.  $R^2$  indicates goodness of fit for linear fits to reverse (red; parentheses indicate  $R^2$  for one maximum value for each individual reversal) and forward (gray) groups. Compare to Figure 2G.

(U and V) RIM  $\text{Ca}^{2+}$ -imaging in worms able to move freely on the imaging pad, after application of tetramisole.

(U) Example trace showing normalized GCaMP/mCherry fluorescence ratio (black) and corresponding crawling speed (green). Pink bars overlay reverse crawling periods.

(V) Event-triggered average of neuronal activity aligned to reversal onset (left) or reversal end (right). Upper and lower traces represent 90<sup>th</sup> and 10<sup>th</sup> percentile of all data, respectively. Number of recorded worms and events are indicated. Vertical line next to each trace indicates  $0.5 \Delta R/R_0$ . Compare to Figure 2H, top row; note different x-axes. (W–X) Two example traces of RIM  $\text{Ca}^{2+}$ -activity in worms confined to the imaging chip (“in chip”) without tetramisole application. High states are observed in all such worms ( $n = 8$ ).

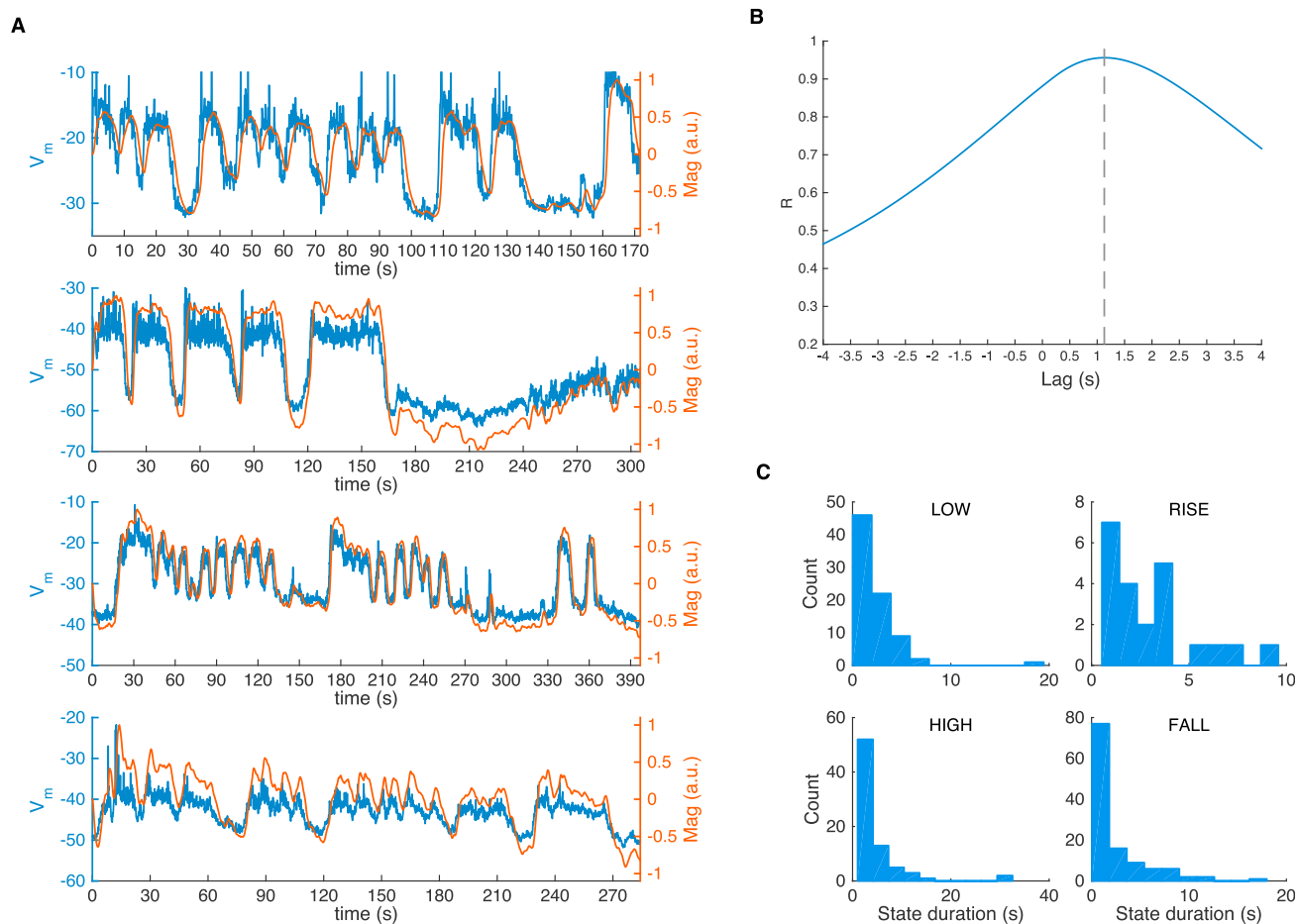


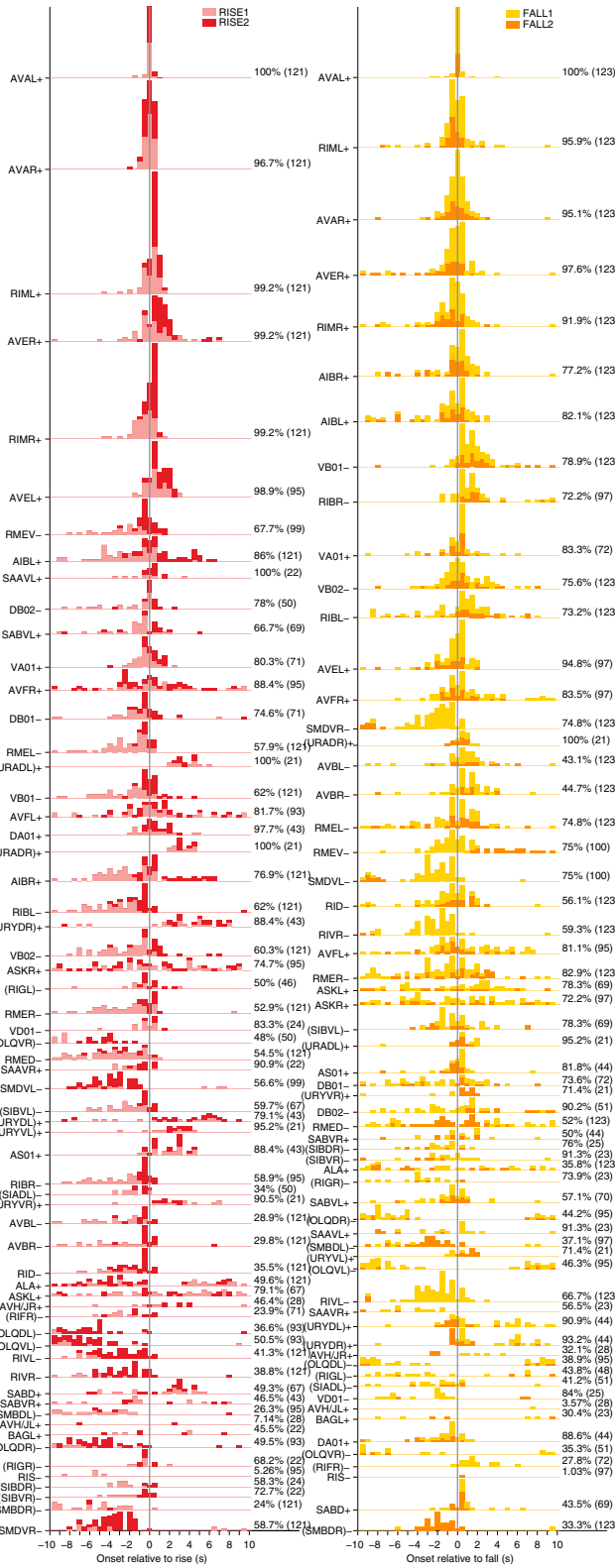
**Figure S4. AVA Membrane Voltage Displays Four Long-Lived Phases Similar to Nuclear GCaMP, Related to Figure 4**

(A) Membrane voltage  $V_m$  in blue and simulated nuclear GCaMP traces in orange. Membrane voltage was measured using the electrophysiological preparation used in reference Lindsay et al. (2011). The nuclear GCaMP signal was simulated by convolving  $V_m$  with an alpha-function filter based on kinetic parameters (.06 s rise  $t_{1/2}$ , 0.28 s fall  $t_{1/2}$ ) of GCaMP5K reported elsewhere (Chen et al., 2013) to simulate a cytoplasmic GCaMP signal, followed by convolution with a single-exponential filter with a time constant of 0.9 s to model the temporal filtering due to nuclear localization. This filter timescale was estimated by fitting the transformation between trial-averaged sensory-evoked transient responses using GCaMP5K and NLS-GCaMP5K from Schrödel et al. (2013) in BAG and URX sensory neurons. Both neurons gave similar estimates.

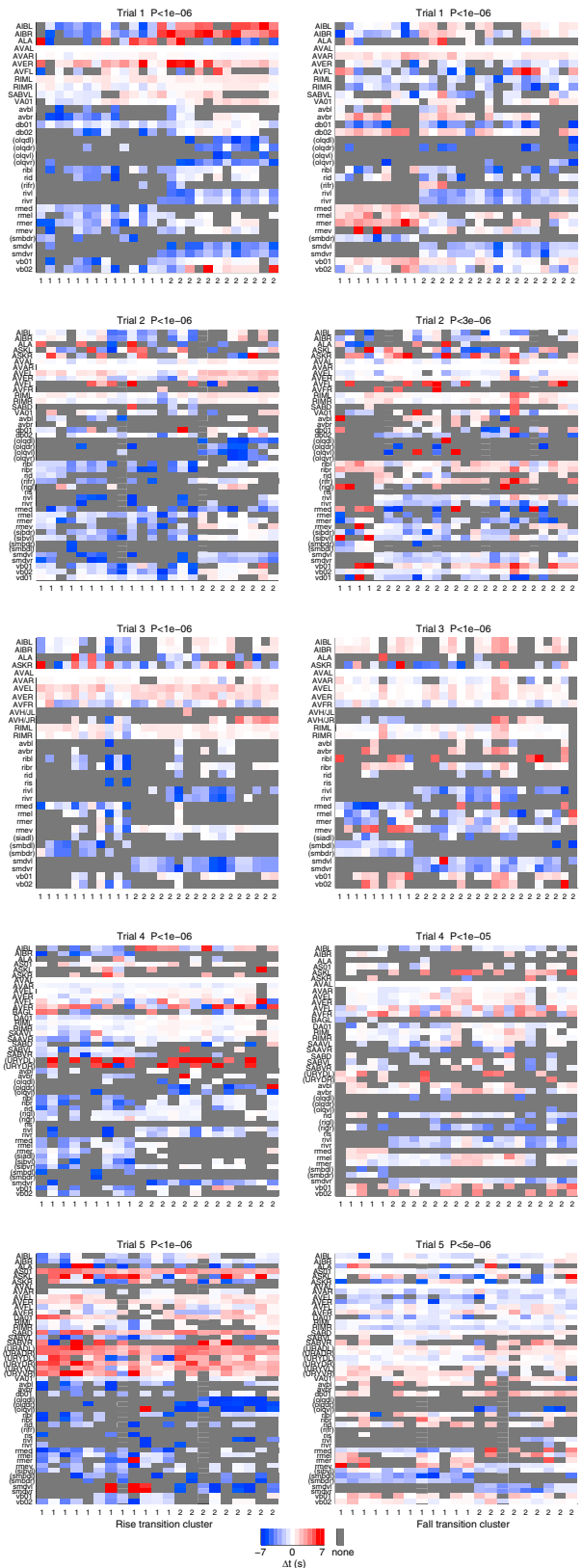
(B) Cross-correlation between  $V_m$  and simulated nuclear GCaMP5K signals yields a lag of 1.16 s. This represents the upper bound of the delay between  $V_m$  and  $Ca^{2+}$  phase onsets.

(C) Distributions of state durations measured from the  $V_m$  traces in (A). Note that all 4 states are long-lived.

**A**



**B**



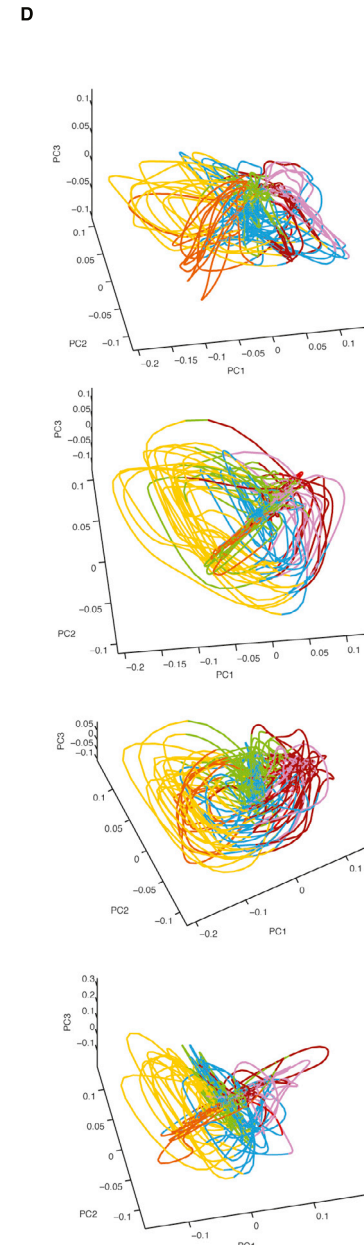
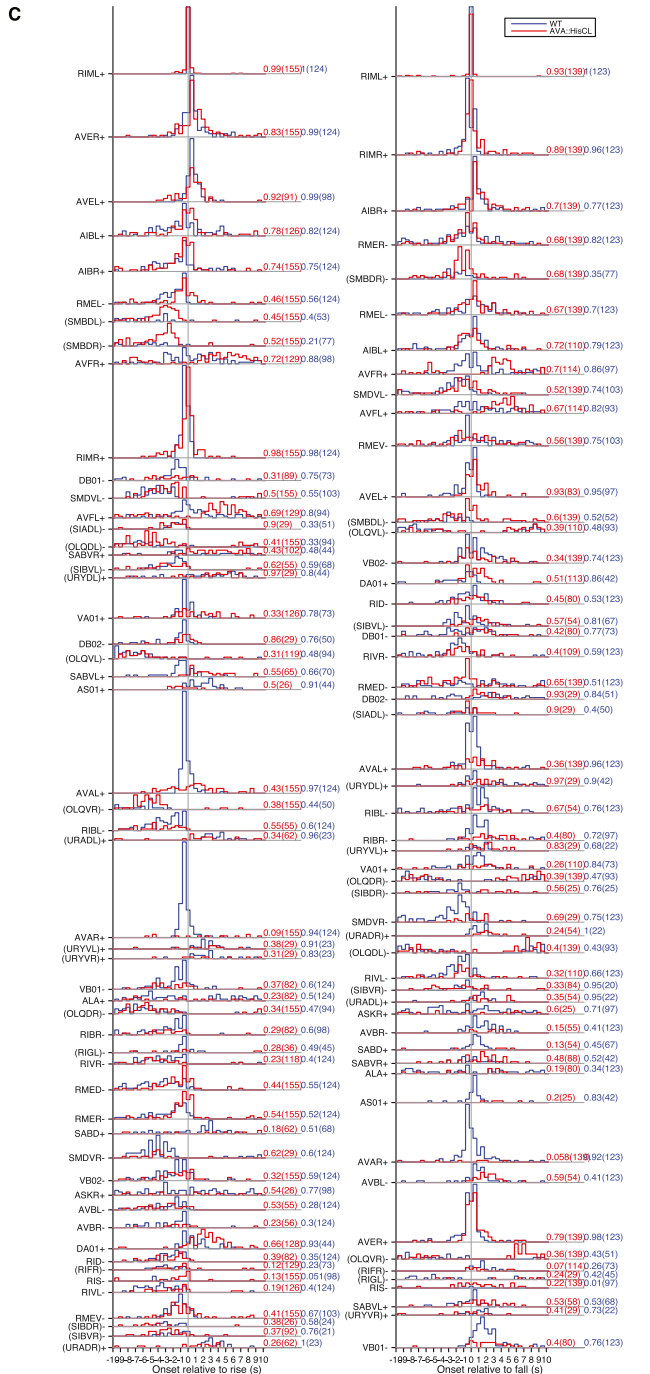
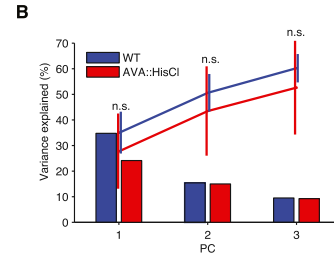
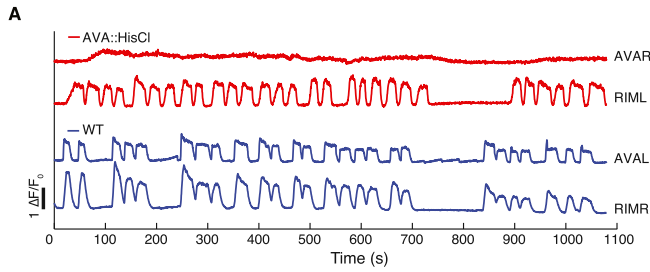
(legend on next page)

---

**Figure S5. Phase Timing Analysis and Clustering, Related to Figure 4**

(A) Cumulative histograms of rise-phase onset times (left column) and fall-phase onset times (right column) for all identified neurons, relative to AVA reference neuron transitions across 5 datasets, limited to transitions within  $-10$  to  $+10$  s of reference transition. Colors are assigned to each histogram point by its cluster membership as indicated by the legend; histograms for each cluster are stacked. Each neuron was assigned a polarity based on the sign of its largest PC contribution, indicated by + or -. Transitions were matched to transitions of the same kind (fall-to-fall, rise-to-rise) for + polarity neurons, whereas transitions were matched to transitions of the opposite kind (fall-to-rise, rise-to-fall) for - polarity neurons. Percentage indicates proportion of transitions in which that neuron displayed a transition in the relative time window, and number in parenthesis indicates the total number of transitions across the trials for which that neuron was identified. Left column shows rise-phase histograms, right column shows fall-phase histograms.

(B) Results of k-means clustering, using  $L_1$  distance, on transition timing vectors for all labeled neurons, for 5 datasets. Each column corresponds to a reference transition, composed of a relative transition time for each labeled neuron, and clustering re-orders the columns into two groups. Grey squares indicate that there was no transition detected in the  $-7$  to  $7$  s window for that neuron, for which a value of  $-10$  was assigned for the purposes of computing vector distances. Left column shows rise-phase transition timing; right column shows fall-phase transition timing. Ambiguous neuron class IDs are in parentheses. Additional candidates: URA: URY; OLQ: URY; URY: OLQ; RIF: AVG/DD01; SMB: SMD/RMF; SIA: SIB; SIB: SIA; RIG: RIF/DB. p values are calculated by a permutation test and indicate the probability that the ratio of the average pairwise inter-cluster distance to the average pairwise intra-cluster distance occurred by chance, under a random cluster assignment.



(legend on next page)

---

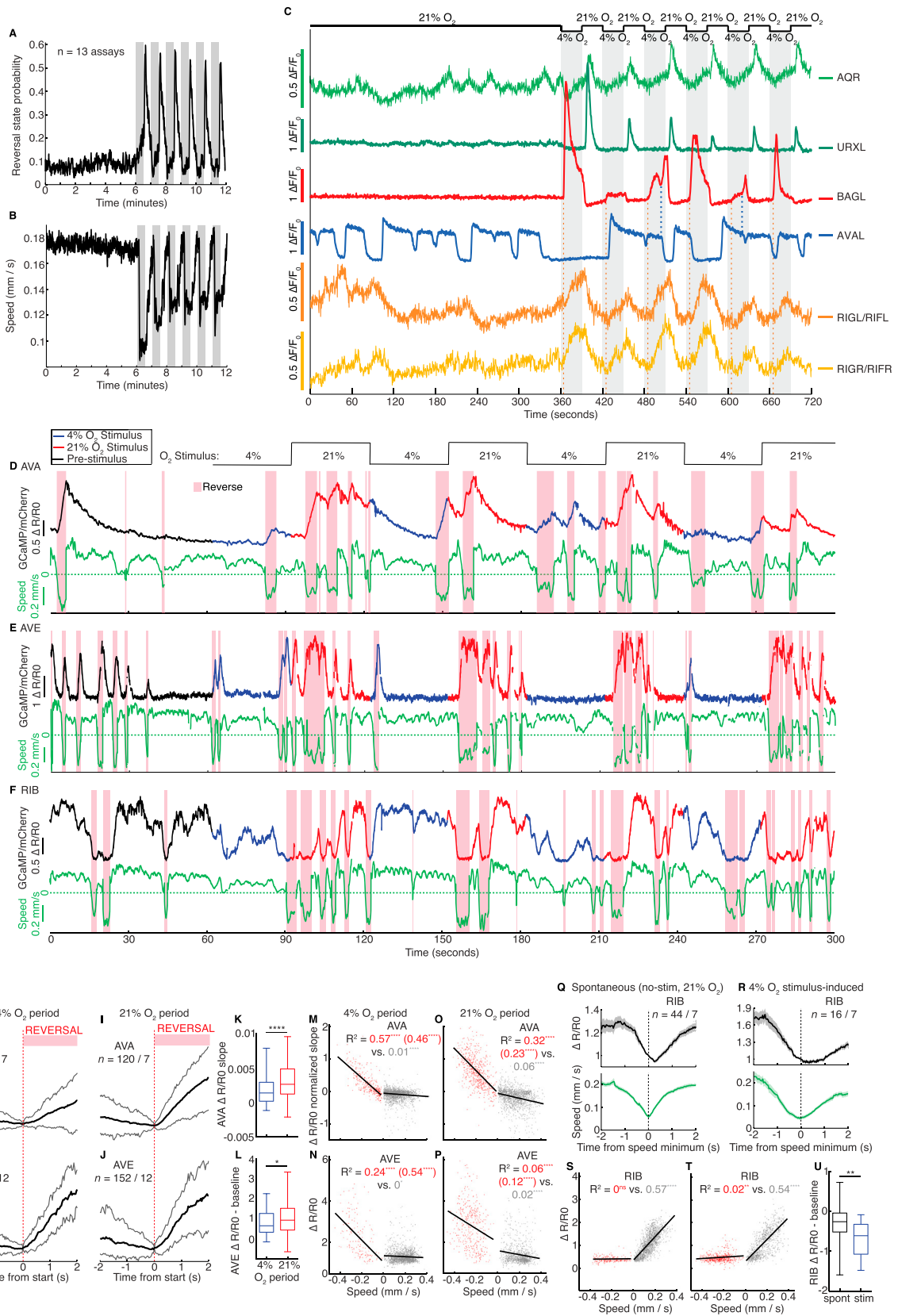
**Figure S6. Phase Relationships Are Preserved Despite AVA Silencing, Related to Figure 5**

(A) HisCl applied to AVA::HisCl worms silenced most transient activity in AVAR while RIM dynamics retained wild-type appearance.

(B) Variance explained of the top 3 PCs in AVA::HisCl (red) versus wild-type (blue), with cumulative variance explained shown as a line, and SEM as vertical lines ( $n = 5$  for both). 3 dimensions still dominated the activity time series in AVA silenced trials.

(C) Cumulative histograms of relative phase transition times similar to Figure S5 for AVA::HisCl worms versus wild-type, using RIML as the timing reference instead of AVAL for both groups, since AVA neurons were inactivated in AVA::HisCl trials. Aside from AVA, most phase relationships to the global brain cycle were intact.

(D) Phase plots of repeated trials from AVA silenced worms.



(legend on next page)

**Figure S7. O<sub>2</sub> Stimulation Probabilistically Modulates Behavior and Brain State, Which Feeds Back onto Sensory Neuron Activity, and Interneurons Are Modified by O<sub>2</sub> Stimulation but Maintain Strict Motor State Relationships, Related to Figure 6**

(A and B) Population behavior assays using the same O<sub>2</sub> stimulation protocol as in Figure 6. Grey bars mark 4% O<sub>2</sub>; all other periods are at 21% O<sub>2</sub>. 20-25 worms per assay; number of assays is indicated.

(A) Reversal state probability is entrained by stimulus.

(B) Average forward crawling speed is also entrained.

(C) Example traces of neuronal activity during O<sub>2</sub> stimulation protocol. Gray bars indicate 4% O<sub>2</sub>. AQR and URX are reliably activated upon O<sub>2</sub> upshifts whereas BAG is activated upon O<sub>2</sub> downshifts. Dashed blue lines mark secondary BAG transients coincident with AVA FALLS. One ventral ganglion neuron class, RIG or RIF, was the only non-sensory neuron found to represent the O<sub>2</sub> stimulus. Using marker lines we confirmed that this neuron class expresses *sra-11* but not *flp-18*, yet this did not allow unambiguous identification. However, the strong synaptic coupling to BAG suggests RIG as the strongest candidate.

(D–U) Ca<sup>2+</sup> imaging in freely moving animals under O<sub>2</sub> stimulation. Data are divided into pre-stimulus (black, constant 21% O<sub>2</sub> after pre-incubation at 21% O<sub>2</sub>), 4% O<sub>2</sub> stimulus (red), and 21% O<sub>2</sub> stimulus (blue) periods.

(D–F) Example traces showing the activities of AVA (D), AVE (E), and RIB (F). Corresponding crawling speed is shown in green. Pink bars overlay reverse crawling periods.

(G–J) Event-triggered average of AVA (G, I) or AVE (H, J) neuronal activity aligned to reversal onset during either 4% O<sub>2</sub> (G–H) or 21% O<sub>2</sub> (I–J) stimulus periods. Number of recorded worms and events is indicated. Vertical line next to each trace indicates 0.25  $\Delta R/R_0$  (G, I) or 1  $\Delta R/R_0$  (H, J).

(K–L), Quantifications of interneuron activities during events shown in (G–J). Boxes show median and 25<sup>th</sup> to 75<sup>th</sup> percentiles, and whiskers show min to max.

(K) Average AVA Ca<sup>2+</sup> signal slope for reversals that occurred during either 4% (blue) or 21% (red) O<sub>2</sub> stimulus periods. Mann-Whitney test  $p < 0.0001$ .

(L) Average AVE Ca<sup>2+</sup> signal change minus pre-reversal baseline for reversals that occurred during either 4% (blue) or 21% (red) O<sub>2</sub> stimulus periods. Mann-Whitney test  $p < 0.05$ .

(M–P) Regression analysis using all AVA and AVE recordings of crawling speed versus normalized Ca<sup>2+</sup>-signal slope (M, O) or absolute Ca<sup>2+</sup> signal (N, P) during either 4% (M–N) or 21% (O–P) O<sub>2</sub> stimulus periods for the indicated neurons. R<sup>2</sup> indicates goodness of fit for linear fits to reverse (red; parentheses indicate R<sup>2</sup> for one maximum value for each individual reversal) and forward (gray) groups. Permutation test p-value: \*\*\*\* $p < 0.0001$  \*\* $p < 0.01$  \* $p < 0.05$  <sup>ns</sup>not significant. Compare to Figures S3I and S3J, respectively. Interestingly, AVE loses its relationship with reverse crawling speed during 21% O<sub>2</sub> stimulation, indicating a more complex effect of stimulus on AVE than on AVA or RIB.

(Q–R) Event-triggered averages of RIB activity ( $\pm$ SEM, upper panels) and crawling speed ( $\pm$ SEM, lower panels) aligned to speed minima of slowing events without reversals, made either spontaneously (Q: constant 21% O<sub>2</sub> after pre-incubation at 21% O<sub>2</sub>) or induced by O<sub>2</sub> downshift (R: event occurs within first 5 s following shift to 4% O<sub>2</sub>). Number of recorded worms and events is indicated.

(S and T) Regression analysis of crawling speed versus absolute Ca<sup>2+</sup> signal for all RIB recordings during either 4% (S) or 21% (T) O<sub>2</sub> stimulus periods. R<sup>2</sup> indicates goodness of fit for linear fits to reverse (red) and forward (gray) groups. Compare to Figure S3L.

(U) RIB Ca<sup>2+</sup> signal change from baseline during slowing events that occurred spontaneously (black) or induced by O<sub>2</sub> downshift (blue). Average Ca<sup>2+</sup> signal was calculated from a 0.5 s window surrounding either the slowing minimum or two seconds earlier (baseline). Quantifications of interneuron activities during events shown in (Q–R). Boxes show median and 25<sup>th</sup> to 75<sup>th</sup> percentiles, and whiskers show min to max. Mann-Whitney test  $p < 0.01$ .

Cell

Supplemental Information

## **Global Brain Dynamics Embed the Motor**

### **Command Sequence of *Caenorhabditis elegans***

Saul Kato, Harris S. Kaplan, Tina Schrödel, Susanne Skora, Theodore H. Lindsay,  
Eviatar Yemini, Shawn Lockery, and Manuel Zimmer

## **Supplemental Experimental Procedures**

### **Whole-brain Ca<sup>2+</sup> imaging of *C. elegans* head ganglia neurons**

Two-layer PDMS microfluidic devices were manufactured as described previously (Zimmer et al., 2009). The chip design was comprised of a curved worm channel to laterally align animals as described previously (Cáceres et al., 2012) with a straight elongation of the channel after the curve to obtain a straight body posture of the worm during imaging. Gas flow (50 ml/min) in the device was controlled using a static gas mixer connected to mass flow controllers (Vögtling Instruments) operated by LabView software. Different O<sub>2</sub> concentrations were balanced with N<sub>2</sub>. The worm channel was connected by Tygon or polyethylene tubing to a reservoir containing nematode growth medium (NGM) and 1 mM tetramisole. Adult worms (carrying zero to four eggs) were picked on food-free NGM agar plates in a drop of NGM with 1mM tetramisole and aspirated into the worm channel. Recordings were started within 5 minutes after removal from food. Illumination and piezo stage were switched on 2 minutes prior to recording. Worms were either imaged for 18 minutes at constant 21% O<sub>2</sub>, or for the stimulus protocol, they were imaged for 12 minutes with the first 6 minutes at 21% O<sub>2</sub> and the remaining 6 minutes with 30 s consecutive shifts between 4% and 21% O<sub>2</sub>. Data was acquired using an inverted spinning disc microscope (UltraViewVoX, PerkinElmer) equipped with an EMCCD camera (C9100-13, Hamamatsu). Read-out area on the camera chip was 150-170 x 512 pixels, translating to a field of view of 50-56 x 170 μm on the sample, which was divided into 11-12 z-planes spaced by 2 μm. These settings allowed an imaging rate of 2.6 – 3 volumes per second. To inhibit AVA in HisCl expressing lines, worms were incubated for 30-45 min on OP50 seeded NGM agar plates including 20 mM histamine (histamine dihydrochloride, Sigma-Aldrich) before loading them into the worm channel filled with NGM containing 10 mM histamine.

## **Electrophysiology**

Records of AVA membrane potential were extracted from a database of current clamp recordings collected but not reported in previous studies. Briefly, recording pipettes were pulled and pressure-polished to achieve resistances of 10–20 M $\Omega$  when filled with normal internal saline. The AVA neuron was identified by targeted expression of tdTomato using the *nmr-1* promoter followed by assessment of the time and voltage dependence of cell-intrinsic currents as described previously (Lindsay et al., 2011). Pulses used to calculate whole-cell capacitance and series resistance were filtered at 50 kHz and sampled at 125 kHz. All cells reported here had a whole cell capacitance of > 0.2 pF. Current-clamp recordings of membrane potential, were filtered at 2 kHz, sampled at 10 kHz and corrected for the liquid junction potential post-hoc. Depending on the resting membrane potential, 0-3 pA of constant negative current was injected to compensate for the large depolarizing effect of the leak conductance generated when patching high input resistance cells (Barry and Lynch, 1991). Internal saline consisted of 143 mM K-gluconate, 1 mM CaCl<sub>2</sub>, 4 mM NaCl, 1 mM MgCl<sub>2</sub>, 10 mM HEPES, 10 mM EGTA, pH 7.2 (KOH). External saline consisted of 5 mM KCl, 10 mM HEPES, 8 mM CaCl<sub>2</sub>, 143 mM NaCl, 30 mM glucose, pH 7.2 (NaOH).

## **Simulation of nuclear GCaMP signals from voltage traces**

To simulate the nuclear GCaMP5K signal that would be generated from an underlying membrane voltage signal, we convolved voltage traces with a kernel based on GCaMP5K dynamical parameters reported elsewhere (Chen et al., 2013), followed by convolution with a single exponential kernel with  $\tau=0.9$  sec, to model the transformation between the cytoplasmic GCaMP signal and a nuclear localized GcaMP signal. This time constant was determined by an optimization procedure, minimizing the difference between trial-averaged nuclear localized GcaMP5K step responses of BAG neurons versus putatively convolved trial-averaged cytoplasmic

GCaMP5K step responses, data taken from (Schrödel et al., 2013). We neglect the transformation between voltage and  $\text{Ca}^{2+}$ , which we expect to be much faster than the other processes and thus not appreciably affect the overall temporal effects.

### **$\text{Ca}^{2+}$ imaging in freely moving animals**

$\text{Ca}^{2+}$  imaging recordings were made using the automatic re-centering system described previously (Faumont et al., 2011). Young adult worms (0-8 eggs) expressed both mCherry and GCaMP in the neuron of interest; mCherry expression was optimized to allow sufficient signal intensities required for efficient tracking, while GCaMP expression was kept relatively low, which in our experience leads to higher dynamic range signals in neurons. Animals were picked and transferred onto a growth medium (NGM) plate to allow crawling away from food, then placed on a NGM agarose pad and sealed in a custom built microscope stage containing an airtight chamber with inlet and outlet connectors for gas flow delivery. Worms were given five minutes to acclimate to the pad and to the 21%  $\text{O}_2$  flow conditions before recordings began. For **Figure 2**, **Figure 3**, and **Figure S3**, each worm was recorded for 3-4 minutes. For **Figure S7**, each worm was recorded for 1 minute at 21%  $\text{O}_2$  prior to either 8 (AVE) or 12 (AVA, RIB) consecutive  $\text{O}_2$  up- and down-shifts lasting 30 s each.

Preparation of homogeneously thick NGM agarose pads required for imaging was achieved as follows: agarose was melted and poured into a ring 2.45 mm thick and 50 mm in diameter and enclosed with glass on both sides to harden into a smooth surface. A ring of 38 mm diameter was pressed onto the agarose to produce an indentation into which a repellent  $\text{CuCl}_2$  (20 mM) solution was pipetted to restrict the worm to the pad center. The pad was placed inside the chamber, which was sealed shut and covered with a 0.55 mm thick glass slide 0.7 mm from the agarose surface. This created a perpendicular homogeneous surface below the flow chamber both

within the working distance of the objective lens. The chamber was then placed into a motorized stage with associated controller (MS-2000-PhotoTrack, Applied Scientific Instrumentation). Images were acquired on an inverted compound microscope (Zeiss Axio Observer.Z1) using two CCD cameras (Evolve 512, Photometrics). Excitation light (470nm and 585nm) was provided by a CoolLED pE excitation system simultaneously using an ET-EGFP/mCherry filter set (59022x, Chroma) and dichroic (59022bs, Chroma). A long-distance 63x objective (Zeiss LD Plan-Neofluar 63x, 0.75 NA) was used to obtain unbinned images at 33 ms exposure time with VisiView software (Visitron Systems GmbH, Germany). A dichroic mirror (620 spxr, Chroma) directed high wavelength mCherry emission to a four-quadrant photomultiplier tube (Hamamatsu) for re-centering. The remaining emission was split by a DualCam DC2 cube (565 lpxr, Photometrics) to each of the two CCD cameras, one for mCherry emission (641/75nm, Brightline) and one for GCaMP emission (520/35nm, Brightline). mCherry emission was further reduced by 50% via a neutral density filter to prevent signal saturation. Simultaneous behavior recordings under infrared illumination (780nm) were made using a CCD camera (Manta Prosilica GigE, Applied Vision Technologies) at 4x magnification and 100 ms exposure time.

GCaMP and mCherry signals were quantified either by custom MATLAB scripts (The MathWorks) if the neuron was the only or brightest cell expressing mCherry or by MetaMorph software (Molecular Devices) if several neurons were labeled. The brighter mCherry signals were used as analysis tracking targets to determine a region of interest (ROI) used to record the dimmer GCaMP signals. Signals were measured as integrated fluorescence over the ROI, subtracting a background value computed per recording, taken from the first frame using the same sized ROI on a region in the worm's head lacking labeled neurons. The GCaMP/mCherry ratio was then divided by an  $R_0$  value calculated within each recording as either the mean ratio over the entire recording (for fluctuating neurons RIB, SMDV, AVB, RMEV, or RID) or

the mean of the lowest 10% of ratio values (for occasional spiking neurons RIM, AVA, AVE, and AIB) to avoid biasing by variability in animal behavior.

Ca<sup>2+</sup> signals used to calculate event-triggered averages had their  $\Delta R/R_0$  values shifted (added or subtracted) such that all events had the same value at  $t = 0$ . RIM and AVA slopes were calculated as de-noised time derivatives as described below. AVA slope and SMDV activity, for **Figures S3I, S7M, S7O** and for **Figure 3E** respectively, were peak-normalized within recordings. For **Figure 3E** head-bend angle was normalized to the standard deviation within each recording. Data in speed versus activity scatterplots were found by binning each individual reverse and forward locomotion period into 0.5 s bins and averaging within bins. To avoid spurious correlations due to coincident rise-phases of Ca<sup>2+</sup> activity and reversal speed, single values for speed and rise-phase slope (RIM, AVA) or magnitude (AVE) were calculated for each reversal by averaging all data above median speed or Ca<sup>2+</sup> activity; R<sup>2</sup> for these data are given in parentheses in each figure panel. Ca<sup>2+</sup> activity data in **Figure 3E** were found by averaging data points within 1.5 s on either side of the head-bend peak angle frame, and control bend Ca<sup>2+</sup> activity data were found using the same procedure on Ca<sup>2+</sup> activity occurring with the head-bend peak found following randomly selected time points during forward movement, as if these random time points were reversal offsets. All p-values for R<sup>2</sup> were determined by bootstrapping: data were randomly permuted and R<sup>2</sup> was calculated 10<sup>6</sup> times, and p-value was calculated as the fraction of R<sup>2</sup> values greater than the R<sup>2</sup> of the non-permuted data. Activity peaks (after peak-normalization) and speed minima in **Figure S3Q** and **S7Q-R** were found using a peak-detection algorithm.

Freely moving + tetramisole recordings were made by applying 1-5mM tetramisole to worms placed on the imaging pad. Freely moving + or - histamine recordings were made by placing worms on food-seeded NGM plates + or - 20mM histamine 30-45

minutes prior to imaging and, in both experimental and control cases, recording them on pads lacking histamine.

### **Behavior tracking in single freely moving animals**

Reversals and omega turns were identified manually, blind to corresponding neural activity data, by examining infrared movies and x-y plots of stage position captured with every  $\text{Ca}^{2+}$  imaging frame. All time points not marked as reversals were considered forward movement for computing speed correlations. Bends where the worm's head touched or nearly touched its tail were classified as omega turns. Body angles were determined using a skeletonization procedure on the infrared movies (Yemini et al., 2013), and the first of nine resulting segment angles was selected as the head-bend angle. The post-reversal head-bend was marked as the first peak in head-bend angle following reversal offset, and often closely or exactly coincided with reversal offset. Ventral vs. dorsal direction was determined by the co-recorded mCherry expression pattern. Speed was calculated according to x-y stage position, smoothed, and marked as negative wherever worms were reversing. Speed minima in **Figure S7Q-R** were found using a peak-detection algorithm on these data.

### **Region of interest (ROI) detection from volumetric $\text{Ca}^{2+}$ -imaging data**

Inter-frame motion was computed for each time step of each image plane using discrete Fourier transform based sub-pixel image registration (Guizar-Sicairos et al., 2008). A reference ROI movie was composed for each image plane by averaging successive blocks of 100 movie frames to reduce noise. Each frame of the reference movie was adaptively thresholded based on the median image brightness plus an offset and median filtered with a 3x3 block to de-noise, then local maxima pixels were found. Local maxima closer than 5 pixels were merged using a greedy algorithm to produce single plane, single frame ROI centers. For each ROI center in each frame, a 5-pixel radius circular ROI was defined. Overlapping ROI areas were

removed using Voronoi tessellation with area shrinkage applied to leave a 0.5 pixel margin between ROIs, thereby leaving a thin frame of pixels not in any ROI to be used for background subtraction described below. ROIs in adjacent reference movie frames were adjoined using a greedy algorithm based on closest distance relative to global inter-frame motion, subject to a maximum x-y acceleration of 5 pixels/frame<sup>2</sup>, to produce time-varying ROIs spanning the time range of the movie for which the ROI center was detectable. To track cells that fell below the detection threshold for spans of time, then reappeared, the positions of ROIs that terminated mid-movie were extrapolated based on the motion of neighboring ROIs within 20 pixels and adjoined to proximate ROIs that appeared mid-movie. Finally, time-varying, multi-plane regions of interest (“4D-ROIs”) were created by adjoining the time-varying ROIs present in adjacent Z-planes with overlapping x-y extent, producing one spacetime voxel set. Ambiguities in the ROI adjoining process were resolved by human judgment during a proof-checking phase. ROIs that identified non-neuronal recording artifacts, such as gut autofluorescence, were removed during this phase. Occasionally, additional neurons were observed that were not identified using the above detection scheme. ROI centers for these neurons were determined by measuring a fixed displacement from an existing ROI nearby and maintaining that relative spatial displacement throughout the recording, and 5-pixel radius, single-Z plane time-varying ROIs were defined for these neurons.

### **Neural time series extraction**

For each 4D-ROI, a single-cell fluorescence intensity  $F$  was computed by taking the average of the brightest 75 voxels at every time point after subtracting a z-plane specific background fluorescence intensity. Background values were computed by averaging pixels not belonging to any ROI (see prior section) within a radius of 16 pixels from the ROI center.  $\Delta F/F_0$  was computed for each neuron with  $F_0$  taken as the mean fluorescence intensity across the trial.

### **Identification of head ganglia neurons**

In each recording we detected 107-131 neurons, covering 55-67% of expected neurons in the imaging area. As previously determined (Schrödel et al., 2013), many neurons remain undetected due to inactivity and low  $\text{Ca}^{2+}$ -levels, as well as lack of neuronal marker expression. Neurons were identified taking into account their anatomical positions, also in relation to surrounding neurons ([www.wormatlas.org](http://www.wormatlas.org)), and their activity patterns. To confirm ambiguous neuron identities, marker lines expressing red fluorophores in neurons of interest were generated and crossed to the imaging line expressing GCaMP5K pan-neuronally in the nucleus (ZIM504). Immediately before recording  $\text{Ca}^{2+}$  traces in these lines one dual-color stack was acquired allowing unambiguous mapping of red fluorophore expression to tracked ROIs. Neurons with identities confirmed by marker expression that showed specific activity patterns and similar anatomical positions could then also be identified in recordings without markers. In some cases neuron identities were ambiguous if no specific marker could be found or if, within the same anatomical region, there were more than one neuron class showing a similar activity pattern. In these cases we denote neuron class identities in parentheses and provide all additional possible candidates in figure legends. All neurons that could not be assigned to a certain class, but had well defined locations and distinct activity patterns were labelled identically across different recordings. Marker lines are provided in the strain list below.

### **Population behavioral assays**

For behavior assays (**Figure 5A**; **Figure S7A-B**) 20-25 adult worms grown on OP50 seeded food plates were picked food free on a NGM agar plate without food. The 36 mm x 36 mm assay arena was confined by Whatman paper soaked with 20 mM  $\text{CuCl}_2$ , a repellent, to prevent worms from leaving the arena. Gas flow (25 ml/min)

was delivered through a transparent plexiglas device with a flow arena of 39 mm x 39 mm x 0.7 mm placed on top of the assay arena and controlled using a static gas mixer connected to mass flow controllers (Vögtling Instruments) operated by LabView software. The 12 min stimulus protocol was the same as for whole-brain imaging experiments (6 min at 21% O<sub>2</sub> followed by six consecutive 30 s shifts to 4% O<sub>2</sub> and back to 21%). During illumination with red LED animals were recorded at 10 fps using a 4 megapixel CCD (Jai) camera and Streampix software. Movie analysis and reversal detection was performed using Matlab-based tracking software as described before (Chalasanani et al., 2007; Ramot et al., 2008; Zimmer et al., 2009). Worms were pre-incubated at constant 21% O<sub>2</sub> on the assay arena for 5 min before recordings were started to accustom them to the gas flow.

For inhibition of AVA in HisCl expressing lines, worms were treated as described in (Pokala et al., 2014). Briefly, they were incubated for 30-45 min on OP50 seeded NGM agar plates including 20 mM histamine (histamine dihydrochloride, Sigma-Aldrich) before picking them on NGM agar assay plates also containing 20 mM histamine.

### **Derivatives and PCA on neural time series data**

PCA was performed on the time derivatives of  $\Delta F/F_0$  neural traces, each normalized by the peak magnitude of corresponding  $\Delta F/F_0$  trace. Total-variation regularization (Chartrand, 2011) was used to compute de-noised time derivatives while preserving accuracy of state transition times to within one frame. This numerical differentiation method was also used during 4-phase analysis of neural  $\Delta F/F_0$  traces and voltage traces. A 3-sample sliding-average filter was applied to each phase plot trajectory to aid visualization, though all analysis was performed on unfiltered traces. Activity traces of the sensory neurons BAG, URX, and AQR were removed from the analysis

in recordings with sensory stimulus applied. Variance explained for each PC in Figures 1E, S2D and S6 was calculated as described previously (Kato, 2014); here, we defined measured data to be the derivatives of the full neural time series, and we defined reconstructed data to be the sums of projections of the derivative time series onto each temporal PC1 to 10.

#### **4-phase segmentation analysis**

Rise phases for neurons were identified as periods when the time derivative was greater than a small threshold, typically 5% of each neuron's full dynamic range, and fall phases for neurons were identified as regions of when the time derivative was less than a small negative threshold, typically 5% of full dynamic range. Using regularization when computing the derivative, in combination with the use of thresholds, rather than simply using any infinitesimal deviation in the derivative from zero, eliminated the presence of spurious short-lived state fluctuations but varying thresholds, up to 10% of the full dynamic range of each neuron, did not significantly affect transition timing relationships. HIGH and LOW phases were then assigned to the remaining periods based on a threshold and lawful phase order, producing a state time series for the neuron in question. For trajectory averaging and generation of phase-registered movies, neuronal time series were registered to a common phase clock by matching phase segment starts and ends followed by linearly interpolating within segments.

#### **Phase timing analysis and clustering**

A set of global transitions, either RISE or FALL onsets, were defined by the transitions of a reference neuron (AVA or RIM in our study), since these transitions were sharper than those of the temporal PCs themselves. For each global transition,

each neuron's state time series was scanned to find the nearest transition of matching or opposite type, depending on the neuron's polarity (see below), and was paired with the reference transition. Neurons were assigned to have positive or negative polarity based on the sign of their PC1 weight, or a negative polarity if their PC2 or PC3 weights exceeded that of PC1. For example, AVB falls were paired with AVA rises, and SMDV falls were paired with AVA falls. The relative delays of each of these paired transitions were composed into a vector thus representing the differential activation/deactivation times of the neurons for that brain-wide transition. Each vector was classified as RISE1 vs. RISE2 and FALL1 vs. FALL2 by *K*-means clustering, which was applied to phase timing vectors for a full trial using Euclidean distance and  $k=2$ . Missing delay values, indicating a neuron lacking a paired transition within  $\pm 7$  seconds of the reference neuron transition, were assigned a value of -10 for the purposes of computing vector distances. In **Figure 4G-H** we estimated the time course of trajectory separation during RISE1 vs. RISE2 and FALL1 vs. FALL2, including their two adjoining full brain cycles. First we calculated a 6 dimensional vector in PCA phase space for each time point of a trajectory by adjoining a vector of the top 3 temporal PCs instantaneous amplitudes with their derivatives to include also directional information. Next, we calculated the Euclidean distances between trajectories for each time point. Clustering ratio, a normalized measure of separation, was defined as the average inter-cluster distance across all possible pairs of vectors divided by the average intra-cluster distance across all possible pairs of vectors within the same cluster, averaged across both clusters. *P*-values indicate the probability by which the resultant or higher distance ratios occurred by random cluster assignment. They were computed using an exact permutation test, shuffling cluster labels and recomputing the clustering ratio,  $10^6$  times.

### **Canonical trajectory calculation and manifold contour surface extraction**

Sets of phase-registered trajectory points, one set for each RISE and each FALL cluster, were extracted at 300 evenly spaced intervals of the phase clocks using linear interpolation, assigning equal clock intervals of  $\pi/2$  to RISE, HIGH, FALL, and LOW segments. Canonical trajectories were produced by taking the means of each set. For each set, a normal plane to the canonical trajectory was determined by the tangent and position of the mean trajectory for that cluster. Points in the set were projected onto this plane, and PCA was performed on their intrinsic plane coordinates to determine the two principal axes for the point set. These principal axes defined a plane ellipse; the length of the axes was set to the square root of the corresponding eigenvalue, so that each ellipse represented a one-standard-deviation contour line. A triangular-mesh tube for each clustered trajectory in 3D PCA space was generated to connect consecutive elliptical rings sampled at 24 points each.

### **Behavioral decoding of whole-brain recordings**

Each time point of the trajectory was first assigned to a global brain cycle HIGH, LOW, RISE1, RISE2, FALL1, or FALL2 segment as described above, then mapped to motor command states as follows. RISE1 and RISE 2 segments were mapped to REVERSAL1 and REVERSAL2 command states respectively. HIGH segments were mapped to SUSTAINED REVERSAL. FALL1 and FALL2 segments were mapped to VENTRAL TURN and DORSAL TURN respectively. LOW segments were mapped to FORWARD, except that RIB fall phases present during global LOW segments were mapped to FORWARD SLOWING command states.

A speed drive was assigned to each point on the trajectory as follows, aside from those in SUSTAINED REVERSAL phases for which no speed drive was inferred. During VENTRAL TURN, DORSAL TURN, FORWARD, and FORWARD SLOWING phases, positive speed drive was taken to be the magnitude of RIB activity, normalized to its most negative value during the trial. During REVERSAL1 and

REVERSAL2 phases, negative speed drive was taken to be the derivative of RIM neuron activity, normalized to its highest value during the trial.

### **Entrainment resampling test**

To improve statistical power, more datasets (n=13 animals for the stimulus group and n=13 animals for the control group) were generated. At least one AVA neuron was identified in each dataset to determine the brain cycle. For entrainment analysis, resampling for group (stimulus and control) P-value computation was performed by applying the stimulus profile with random phase shifts to either the pre-stimulus period (0 to 6 min) or the stimulus period (6-12 min) to each dataset's state time series, then trial-averaged to produce a 12 point (binning 5 s) time series  $p(t)$ , like in **Figure 6C**. The procedure was repeated  $10^6$  times. The test statistic computed for each sample was the accumulated finite difference symmetrized around the midpoint stimulus change time:

$$\sum_{t=2}^6 p(t) - p(t-1) - \sum_{t=8}^{12} p(t) - p(t-1)$$

which results in high values for data oscillating in phase with the stimulus profile and which results in small values for non-entrained, i.e. random or monotonically drifting data.

### **Statistical tests**

Unless otherwise stated in the figure legends, all p-values of statistical quantities were computed using permutation tests performed by random relabeling of experimental groups or cluster assignments. Following standard statistical procedure, p-values indicated the probability that the measured or greater value of a

given test statistic would occur by drawing from an empirically generated distribution of randomly labelled data.

All computations were performed using custom code in MATLAB.

### Strains

Strain name	Experiment	Genotype	Construct (pasmid no.) injection concentrations	Reference for promoter expression pattern
ZIM458	RIM freely-moving imaging	<i>mzmEx299; lite-1(xu7)</i>	<i>Pcex-1::mCherry</i> (pHK19) 50 ng/μL <i>Pcex-1::GCaMP5K</i> (pHK21) 50 ng/μL	(Cohen et al., 2009)
ZIM347	AVA & RIM freely-moving imaging	<i>mzmEx243; lite-1(xu7)</i>	<i>Pflp-18::mCherry</i> (pHK48) 30 ng/μL <i>Pflp-18::GCaMP5K</i> (pRL62) 30 ng/μL	(Cohen et al., 2009)
ZIM601	AVE freely-moving imaging	<i>mzmEx389; lite-1(xu7)</i>	<i>Popt-3::tagRFP</i> (pHK146) 50 ng/μL <i>Popt-3::GCaMP5K</i> (pRL66) 50 ng/μL	www.wormatlas.org
ZIM519	AIB freely-moving imaging	<i>mzmEx337; lite-1(xu7)</i>	<i>Pnpr-9::mCherry</i> (pHK105) 50 ng/μL <i>Pinx-1::GCaMP5K</i> (pHK55) 50 ng/μL	<i>Pnpr-9</i> : (Luedtke et al., 2010) <i>Pinx-1</i> : (Altun et al., 2009)
ZIM583	RIB freely-moving imaging	<i>mzmEx376; lite-1(xu7)</i>	<i>Psto-3::mCherry</i> (pHK129) 20 ng/μL <i>Psto-3::G-CaMP6FOPT</i> (pHK130) 5 ng/μL	www.wormatlas.org
ZIM498	AVB freely-moving imaging	<i>mzmEx324; lite-1(xu7)</i>	<i>Psra-11::mCherry</i> (pHK56) 50 ng/μL <i>Psra-11::GCaMP5K</i> (pHK57) 50 ng/μL	(Troemel et al., 1995)
ZIM698	RMEV freely-moving imaging	<i>mzmEx437; lite-1(xu7)</i>	<i>Pser-2prom2::NLSwCherryNLS</i> (pHK163) 50 ng/μL <i>Pser-2prom2::NLSGCaMP6FcodoptNLS</i> (pHK164) 10 ng/μL	(Tsalik et al., 2003)
ZIM813	SMDV freely-moving imaging	<i>mzmEx488; lite-1(xu7)</i>	Complex array using bacterial DNA <i>Punc-7S::mCherry</i> (pHK173) 5 ng/μL <i>Punc-7S::GCaMP6Fcodopt</i> (pHK189) 2 ng/μL	(Starich et al., 2009)
ZIM814	RIM freely-moving imaging + AVAHisCl	<i>mzmEx299; kyEx4863; lite-1(xu7)</i>	<i>Pcex-1::mCherry</i> (pHK19) 50 ng/μL <i>Pcex-1::GCaMP5K</i> (pHK21) 50 ng/μL <i>Prig-3::HisCl1::SL2::mCherry</i> (pNP471) 50 ng/μL	<i>Prig-3</i> : (Pokala et al., 2014)
ZIM660	RIM freely-moving nuclear imaging	<i>mzmEx419; lite-1(xu-7)</i>	<i>Pcex-1::NLSwCherryNLS</i> (pHK141) 25 ng/μL <i>Pcex-1::NLSGCaMP5K</i> (pHK162) 37.5 ng/μL	(Cohen et al., 2009)
ZIM504	Whole-brain	<i>mzmEx199;</i>	<i>Punc-31::NLSGCaMP5K</i> (pTS36)	(Schrödel et al.,

	imaging	<i>lite-1 (xu7)</i>	30ng/μL; <i>Punc-122::gfp</i> 15ng/μL	2013)
ZIM756	Whole-brain imaging AVAHisCl	<i>mzmEx199; kyEx4863; lite-1 (xu7)</i>	<i>Punc-31::NLSGCaMP5K</i> (pTS36) 30ng/μL; <i>Punc-122::gfp</i> 15ng/μL; <i>Prig-3::HisCl1::SL2::mCherry</i> (pNP471) 50 ng/μL	<i>Prig-3</i> : (Pokala et al., 2014)
ZIM871	Whole brain imaging SMDV AVE marker	<i>mzmEx199; mzmEx536; lite-1 (xu7)</i>	<i>Punc-31::NLSGCaMP5K</i> (pTS36) 30ng/μL; <i>Punc-122::gfp</i> 15ng/ul <i>Punc-7S::mCherry::His58</i> (pHK174) 50ng/μL	<i>Punc-7S</i> : (Starich et al., 2009)
ZIM651	Whole brain imaging AIB marker	<i>mzmEx199; mzmEx412; lite-1 (xu7)</i>	<i>Punc-31::NLSGCaMP5K</i> (pTS36) 30ng/μL; <i>Punc-122::gfp</i> 15ng/ul <i>Pinx-1::NLSwCherryNLS</i> (pHK140) 30ng/μL <i>Punc-122::DsRed</i> 20ng/μL	<i>Pinx-1</i> : (Altun et al., 2009)
ZIM650	Whole brain imaging RIM marker	<i>mzmEx199; mzmEx411; lite-1 (xu7)</i>	<i>Punc-31::NLSGCaMP5K</i> (pTS36) 30ng/μL; <i>Punc-122::gfp</i> 15ng/ul <i>Pcex-1::NLSwCherryNLS</i> (pHK141) 25ng/μL ; <i>Punc-122::DsRed</i> 20ng/μL	(Cohen et al., 2009)
ZIM730	RIB marker	<i>mzmEx447; lite-1 (xu7)</i>	<i>Psto-3::NLSwCherryNLS</i> (pTS105) 30ng/μL + <i>Punc-122::dsRed</i> 15ng/μL	www.wormatlas.org
ZIM895	Whole brain imaging AVB marker	<i>mzmEx199; mzmEx432; lite-1 (xu7)</i>	<i>Punc-31::NLSGCaMP5K</i> (pTS36) 30ng/μL; <i>Punc-122::gfp</i> 15ng/μL <i>Psra-11::NLSwCherryNLS</i> (pHK143) 25ng/μL + <i>Punc-122::dsRed</i> 15ng/μL	<i>Psra-11</i> : (Troemel et al., 1995)
ZIM888	Whole brain imaging ASK marker	<i>mzmEx199; mzmEx545; lite-1 (xu7)</i>	<i>Punc-31::NLSGCaMP5K</i> (pTS36) 30ng/μL+ <i>Punc-122::gfp</i> 15ng/μL <i>Psrbc-64::NLSwCherryNLS</i> (pTS113) 25ng/μL + <i>Punc-122::dsRed</i> 15ng/μL	<i>Psrbc-64</i> : (Kim et al., 2009)
ZIM764	Whole brain imaging AWB AWC marker	<i>mzmEx199; mzmEx433; lite-1 (xu7)</i>	<i>Punc-31::NLSGCaMP5K</i> (pTS36) 30ng/μL+ <i>Punc-122::gfp</i> 15ng/μL <i>Podr-1::NLSwCherryNLS</i> (pTS104) 40ng/μL + <i>Punc-122::dsRed</i> 15ng/μL	<i>Podr-1</i> : (Yu et al., 1997)
ZIM759	Whole brain imaging AVH/J marker	<i>mzmEx199; mzmEx446; lite-1 (xu7)</i>	<i>Punc-31::NLSGCaMP5K</i> (pTS36) 30ng/μL; <i>Punc-122::gfp</i> 15ng/μL <i>Phlh-34::NLSwCherryNLS</i> (pSS22) 20ng/μL + <i>Punc-122::dsRed</i> 15ng/μL	<i>Phlh-34</i> : (Cunningham et al., 2012)
ZIM773	Whole brain imaging AVF marker	<i>mzmEx199; mzmEx367; lite-1 (xu7)</i>	<i>Punc-31::NLSGCaMP5K</i> (pTS36) 30ng/μL; <i>Punc-122::gfp</i> 15ng/μL <i>Ppdfr-1::NLSwCherryNLS</i> (pTS92) 15ng/μL; <i>Punc-122::dsRed</i> 20ng/μL	<i>Ppdfr-1</i> : (Barrios et al., 2012)
ZIM811	Whole brain imaging OLQ marker	<i>mzmEx199; mzmEx480; lite-1 (xu7)</i>	<i>Punc-31::NLSGCaMP5K</i> (pTS36) 30ng/μL+ <i>Punc-122::gfp</i> 15ng/μL <i>Pocr-4::NLSwCherryNLS</i> (pAN17) 30ng/μL <i>Punc-122::dsRed</i> 15ng/μL	<i>Pocr-4</i> : (Tobin et al., 2002)

## **Primers**

<b>Promoter</b>	<b>P1 (5'-&gt;3')</b>	<b>P2 (5'-&gt;3')</b>
<i>Pcex-1</i>	ATGAACATTCCATGGGTTGTG	CACCAACCTGGAAAACCTACAC
<i>Pflp-18</i>	TCTGTCACATACTGCTCGAA	GTTGCWTGTCTAACCCCTGAA
<i>Popt-3</i>	GATAAAAATAACAGAATTAG	GGGAGAGGCGGAATTAATTT
<i>Pnpr-9</i>	GTTGAATCATCCAAAACGGT	CAACGACATTTCCAGGAAG
<i>Pinx-1</i>	GACAAGAAGTCAATGAAAAC	CAGATTCATAACTGTCTATG
<i>Psto-3</i>	AGCCAAACCAAGTGAGAAG	CACCAAATCATCACGCTG
<i>Psra-11</i>	GTTTTGCACAAATCCCCTGT	TTGTGTGTTGCGGAGATGTG
<i>Pser-2prom2</i>	GTCTGGTAAGTTGAACATGGAGTC	TTTTGCAAATTAATTGAGGCTGC
<i>Punc-7S</i>	ACCGTCGACAGTCCATCGAA	GGAAGACGTGTTTGATAGCG
<i>Punc-31</i>	GTGCATTTTTGGCATTTTCC	AACAAGGAGACTTCAAATTG
<i>Psrbc-64</i>	TGCAAGAGTCGGTTGCAAATA	TTTTCAGACTGTGACAAGAAAAC
<i>Podr-1(Pgcy-10)</i>	AGCTTTTCAGCATTGAGGG	CGAAGAGCACACCAATTCA
<i>Phlh-34</i>	TGAGCAACTTTCTCTTGAACA	TTCTCAAGTGTTATAAGTCAAG
<i>Ppdfr-1 (proximal)</i>	CCCACCCTCCAAATGTCTTG	GGTGACGTGGCATCCGCCAT
<i>Pocr-4</i>	ACTCATCGACCAGGAATAAC	ATTAATACAAGTTAGATTGAGAG

**Table S1**

Neuron class	Ablation effect	Inhibition effect	Activation effect
AIA	R <sup>*a</sup>		
AIB	F <sup>bc</sup> , T <sup>bc</sup>	F <sup>d</sup>	R <sup>cd</sup>
AIY	R <sup>b</sup> , T <sup>b</sup>	R <sup>d</sup> , T <sup>d</sup>	F <sup>d</sup> , T <sup>d</sup>
AIZ	F <sup>b</sup> , T <sup>e</sup>	F <sup>*a</sup>	R <sup>*a</sup> , T <sup>d</sup>
AVA	F <sup>bcd</sup>		R <sup>g</sup>
AVB	R <sup>h</sup>		
AVD	F <sup>h</sup>		
DVA	R <sup>h</sup>		
RIA	F <sup>b</sup>		
RIB	R <sup>i</sup> , F <sup>b</sup>	⊖ <sup>*a</sup>	F <sup>*a</sup>
RIM	R <sup>bi</sup>	R <sup>*c</sup>	R <sup>i</sup>
RIV	T <sup>b</sup>		
RMD	R <sup>b</sup>		
RME	T <sup>b</sup>		T <sup>d</sup>
SIB	F <sup>b</sup>		
SMB	T <sup>b</sup>		T <sup>d</sup>
SMD	R <sup>b</sup> , T <sup>b</sup>		

**Table S1. Single-interneuron manipulations in previous studies nearly always affect reversal frequency and/or turning, related to Figure 1.** Literature review of single interneuron perturbations that affect spontaneous reversals and turns. Listed are the effects of cell ablations, inhibition via Archaelrhodopsin or Halorhodopsin, and activation by Channelrhodopsin; R = increased reversal frequency, F = decreased reversal frequency, T = turning affected, ⊖ = no effect. \*Experiment performed on food. <sup>a</sup>(Li et al., 2014). <sup>b</sup>(Gray et al., 2005). <sup>c</sup>(Piggott et al., 2011). <sup>d</sup>(Kocabas et al., 2012). <sup>e</sup>(Iino and Yoshida, 2009). <sup>f</sup>(Chalfie et al., 1985). <sup>g</sup>(Schmitt et al., 2012). <sup>h</sup>(Rakowski et al., 2013). <sup>i</sup>(Tsalik and Hobert, 2003). <sup>j</sup>(Gordus et al., 2015). For additional functional studies, see (Kawano et al., 2011) and (Luo et al., 2014).

## **Supplemental References**

- Altun, Z.F., Chen, B., Wang, Z.-W., and Hall, D.H. (2009). High resolution map of Caenorhabditis elegans gap junction proteins. *Developmental dynamics : an official publication of the American Association of Anatomists* 238, 1936-1950.
- Barrios, A., Ghosh, R., Fang, C., Emmons, S.W., and Barr, M.M. (2012). PDF-1 neuropeptide signaling modulates a neural circuit for mate-searching behavior in *C. elegans*. *Nature Neuroscience* 15, 1675-7682.
- Barry, P.H., and Lynch, J.W. (1991). Liquid junction potentials and small cell effects in patch-clamp analysis. *The Journal of membrane biology* 121, 101-117.
- Cáceres, I.d.C., Valmas, N., Hilliard, M.A., and Lu, H. (2012). Laterally Orienting *C. elegans* Using Geometry at Microscale for High-Throughput Visual Screens in Neurodegeneration and Neuronal Development Studies. *PLoS ONE* 7, e35037.
- Chalasani, S.H., Chronis, N., Tsunozaki, M., Gray, J.M., Ramot, D., Goodman, M.B., and Bargmann, C.I. (2007). Dissecting a circuit for olfactory behaviour in *Caenorhabditis elegans*. *Nature* 450, 63-70.
- Chalfie, M., Sulston, J.E., White, J.G., Southgate, E., Thomson, J.N., and Brenner, S. (1985). The neural circuit for touch sensitivity in *Caenorhabditis elegans*. *The Journal of neuroscience : the official journal of the Society for Neuroscience* 5, 956-964.
- Chartrand, R. (2011). Numerical Differentiation of Noisy, Nonsmooth Data. *ISRN Applied Mathematics* 2011, 1-11.
- Chen, T.-W., Wardill, T.J., Sun, Y., Pulver, S.R., Renninger, S.L., Baohan, A., Schreiter, E.R., Kerr, R.A., Orger, M.B., Jayaraman, V., *et al.* (2013). Ultrasensitive fluorescent proteins for imaging neuronal activity. *Nature* 499, 295-300.
- Cohen, M., Reale, V., Olofsson, B., Knights, A., Evans, P., and de Bono, M. (2009). Coordinated Regulation of Foraging and Metabolism in *C. elegans* by RFamide Neuropeptide Signaling. *Cell Metabolism* 9, 375-385.
- Cunningham, K.A., Hua, Z., Srinivasan, S., Liu, J., Lee, B.H., Edwards, R.H., and Ashrafi, K. (2012). AMP-Activated Kinase Links Serotonergic Signaling to Glutamate Release for Regulation of Feeding Behavior in *C. elegans*. *Cell Metabolism* 16, 113-121.
- Faumont, S., Rondeau, G., Thiele, T.R., Lawton, K.J., McCormick, K.E., Sottile, M., Griesbeck, O., Heckscher, E.S., Roberts, W.M., Doe, C.Q., *et al.* (2011). An image-free opto-mechanical system for creating virtual environments and imaging neuronal activity in freely moving *Caenorhabditis elegans*. *PLoS ONE* 6, e24666.

Gordus, A., Pokala, N., Levy, S., Flavell, S.W., and Bargmann, C.I. (2015). Feedback from network states generates variability in a probabilistic olfactory circuit. *Cell* *161*, 215-227.

Gray, J.M., Hill, J.J., and Bargmann, C.I. (2005). A circuit for navigation in *Caenorhabditis elegans*. *Proceedings of the National Academy of Sciences of the United States of America* *102*, 3184-3191.

Guizar-Sicairos, M., Thurman, S.T., and Fienup, J.R. (2008). Efficient subpixel image registration algorithms. *Optics letters* *33*, 156-158.

Iino, Y., and Yoshida, K. (2009). Parallel Use of Two Behavioral Mechanisms for Chemotaxis in *Caenorhabditis elegans*. *Journal of Neuroscience* *29*, 5370-5380.

Kawano, T., Po, M.D., Gao, S., Leung, G., Ryu, W.S., and Zhen, M. (2011). An Imbalancing Act: Gap Junctions Reduce the Backward Motor Circuit Activity to Bias *C. elegans* for Forward Locomotion. *Neuron* *72*, 572-586.

Kato, S., Xu, Y., Cho, C.E., Abbott, L.F., and Bargmann, C.I. (2014). Temporal responses of *C. elegans* chemosensory neurons are preserved in behavioral dynamics. *Neuron* *81*, 616-628.

Kim, K., Sato, K., Shibuya, M., Zeiger, D.M., Butcher, R.A., Ragains, J.R., Clardy, J., Touhara, K., and Sengupta, P. (2009). Two chemoreceptors mediate developmental effects of dauer pheromone in *C. elegans*. *Science (New York, NY)* *326*, 994-998.

Kocabas, A., Shen, C.-H., Guo, Z.V., and Ramanathan, S. (2012). Controlling interneuron activity in *Caenorhabditis elegans* to evoke chemotactic behaviour. *Nature* *490*, 273-277.

Li, Z., Liu, J., Zheng, M., and Xu, X.Z.S. (2014). Encoding of both analog- and digital-like behavioral outputs by one *C. elegans* interneuron. *Cell* *159*, 751-765.

Lindsay, T.H., Thiele, T.R., and Lockery, S.R. (2011). Optogenetic analysis of synaptic transmission in the central nervous system of the nematode *Caenorhabditis elegans*. *Nature Communications* *2*, 306.

Luedtke, S., O'Connor, V., Holden-Dye, L., and Walker, R.J. (2010). The regulation of feeding and metabolism in response to food deprivation in *Caenorhabditis elegans*. *Invertebrate Neuroscience* *10*, 63-76.

Luo, L., Wen, Q., Ren, J., Hendricks, M., Gershow, M., Qin, Y., Greenwood, J., Soucy, E.R., Klein, M., Smith-Parker, H.K., *et al.* (2014). Dynamic Encoding of Perception, Memory, and Movement in a *C. elegans* Chemotaxis Circuit. *Neuron* *82*, 1115-1128.

Piggott, B.J., Liu, J., Feng, Z., Wescott, S.A., and Xu, X.Z.S. (2011). The neural circuits and synaptic mechanisms underlying motor initiation in *C. elegans*. *Cell* *147*, 922-933.

Pokala, N., Liu, Q., Gordus, A., and Bargmann, C.I. (2014). Inducible and titratable silencing of *Caenorhabditis elegans* neurons in vivo with histamine-gated chloride channels. *Proceedings of the National Academy of Sciences* 111, 2770-2775.

Rakowski, F., Srinivasan, J., Sternberg, P.W., and Karbowski, J. (2013). Synaptic polarity of the interneuron circuit controlling *C. elegans* locomotion. *Frontiers in computational neuroscience* 7.

Ramot, D., Johnson, B.E., Berry, T.L., Carnell, L., and Goodman, M.B. (2008). The Parallel Worm Tracker: a platform for measuring average speed and drug-induced paralysis in nematodes. *PLoS ONE* 3, e2208.

Schmitt, C., Schultheis, C., Pokala, N., Husson, S.J., Liewald, J.F., Bargmann, C.I., and Gottschalk, A. (2012). Specific expression of channelrhodopsin-2 in single neurons of *Caenorhabditis elegans*. *PLoS ONE* 7, e43164.

Schrödel, T., Prevedel, R., Aumayr, K., Zimmer, M., and Vaziri, A. (2013). Brain-wide 3D imaging of neuronal activity in *Caenorhabditis elegans* with sculpted light. *Nature methods* 10, 1013-1020.

Starich, T.A., Xu, J., Skerrett, I.M., Nicholson, B.J., and Shaw, J.E. (2009). Interactions between innexins UNC-7 and UNC-9 mediate electrical synapse specificity in the *Caenorhabditis elegans* locomotory nervous system. *Neural Development* 4, 16-28.

Tobin, D., Madsen, D., Kahn-Kirby, A., Peckol, E., Moulder, G., Barstead, R., Maricq, A., and Bargmann, C. (2002). Combinatorial expression of TRPV channel proteins defines their sensory functions and subcellular localization in *C. elegans* neurons. *Neuron* 35, 307-318.

Troemel, E.R., Chou, J.H., Dwyer, N.D., Colbert, H.A., and Bargmann, C.I. (1995). Divergent seven transmembrane receptors are candidate chemosensory receptors in *C. elegans*. *Cell* 83, 207-218.

Tsalik, E.L., and Hobert, O. (2003). Functional mapping of neurons that control locomotory behavior in *Caenorhabditis elegans*. *Journal of neurobiology* 56, 178-197.

Tsalik, E.L., Niacaris, T., Wenick, A.S., Pau, K., Avery, L., and Hobert, O. (2003). LIM homeobox gene-dependent expression of biogenic amine receptors in restricted regions of the *C. elegans* nervous system. *Developmental biology* 263, 81-102.

Yemini, E., Jucikas, T., Grundy, L.J., Brown, A.e.E.X., and Schafer, W.R. (2013). A database of *Caenorhabditis elegans* behavioral phenotypes. *Nature methods*, 1-7.

Yu, S., Avery, L., Baude, E., and Garbers, D.L. (1997). Guanylyl cyclase expression in specific sensory neurons: a new family of chemosensory receptors. *Proceedings of the National Academy of Sciences of the United States of America* 94, 3384-3387.

Zimmer, M., Gray, J.M., Pokala, N., Chang, A.J., Karow, D.S., Marletta, M.A., Hudson, M.L., Morton, D.B., Chronis, N., and Bargmann, C.I. (2009). Neurons detect increases and decreases in oxygen levels using distinct guanylate cyclases. *Neuron* 61, 865-879.